Particle self-neutralization for highly efficient deep lung drug delivery via bipolar electrohydrodynamic atomization

Van Canh Doan [a],*, Ngoc Luan Mai [a], Cuong Hung Luu [b], Donglin Cai [c], Wendong Gao [d], Trung Hieu Vu [a], Hoai Duc Vu [a], Thi Van Anh Hoang [a], Duc Khanh Tran [a], Dzung Dao [a], Hang Thu Ta [b], Yin Xiao [c], Peter Woodfield [a], Van Thanh Dau [a],**

[a] School of Engineering and Built Environment, Griffith University, Queensland, Australia
[b] School of Environment and Science, Griffith University, QLD, Australia
[c] School of Medicine and Dentistry, Griffith University, QLD, Australia
[d] Central Analytical Research Facility, Queensland University of Technology, Queensland, Australia

ARTICLE INFO

ABSTRACT

Electrohydrodynamic atomization (EHDA) technology is showing great promise as a more flexible and controllable alternative to conventional nebulizers and inhalers for inhalation-based drug delivery. However, its application is limited by low flow rates and the excessive surface charge on particles, which restricts deep lung deposition. In this study, we introduce a novel bipolar EHDA device, designed for pulmonary drug delivery. This device uses two oppositely charged nozzles to generate self-neutralizing micro/nano particles ideal for inhalation. Experimental and computational investigations confirm the formation of a stable dual-cone jet and efficient neutral particle production at a flow rate of 10 ml/h, which, for the first time in the literature, is comparable with current commercial nebulizers. The polymeric particles exhibit mean aerodynamic diameters 2.65 μm, suitable for deep lung deposition, minimal residual charge, and consistent performance across repeated trials. Furthermore, curcumin-loaded polymeric particles show favorable characteristics including high drug encapsulation, sustained release, and biocompatibility. Deposition testing using an Andersen cascade impactor demonstrated excellent targeting of the deep lung region with minimal drug loss. These results confirm the potential of bipolar EHDA as a compact, high-throughput, and non-invasive solution for pulmonary drug delivery.

1. Introduction

In recent years, drugs in the form of micro/nanosized particles have demonstrated significant advantages, including improved bioavailability of poorly water-soluble therapeutics [1–3], enhanced cellular internalization [4–6], and extended drug retention time in the lungs [7–9]. Delivering drugs into the lungs by inhaling micro/nanosized particles has been shown to effectively mitigate most side effects commonly associated with oral or injectable medications [10–12]. The lungs, with their extensive network of alveoli (300–400 million epithelial cells and a total surface area of up to 70–140 m^2), high capillary density, abundant blood flow, and highly permeable capillaries distributed across adjacent alveoli, provide an ideal pathway for drug absorption through the alveolar surface into circulation [13]. This structure offers significant advantages for pulmonary drug delivery or even systemic delivery, including (i) high drug absorption efficiency, leading to lower required doses and fewer side effects; (ii) suitability for drugs that are sensitive to the gastrointestinal tract and/or liver, avoiding gastric absorption and portal circulation [14]; (iii) faster therapeutic action; and (iv) a lower risk of infection than intravenous or intramuscular injections do [14,15]. As a result, pulmonary drug delivery has been employed to treat various lung-related diseases, such as lung cancer, cystic fibrosis, chronic obstructive pulmonary disease (COPD), asthma, tuberculosis (TB), respiratory allergies, and allergic respiratory diseases (e.g., rhinoconjunctivitis with or without asthma) [16,17]. Additionally, it has been used for systemic treatments, such as the delivery of insulin for diabetes management and peptide-loaded nanoparticles for heart failure treatment [18].

In general, the development process of micro/nanoparticles for pulmonary drug delivery consists of two steps: (i) creation of drug-

---

loaded particles and (ii) aerosolization of drug-loaded particles into the lungs. To effectively deliver drugs into the lungs, drug-loaded particles must overcome two primary physical barriers: particle size (aerodynamic diameter) and surface charge [19,20]. Particles with diameters larger than 5 μm typically deposit in the upper respiratory tract, such as the mouth and oropharynx. Particles smaller than 5 μm can penetrate deeper into smaller airways through three primary mechanisms: inertial impaction, sedimentation, and diffusion. Inertial impaction, which affects particles in the 3–5 μm range, can be influenced by hyperventilation. Particles between 1 and 3 μm in size are deposited by gravity (sedimentation) and are influenced by breath holding. For particles smaller than 1 μm, deposition occurs via diffusion driven by Brownian motion [21–24]. Regarding particle charge, negatively charged or neutral particles are more likely to reach the deep lung regions, such as the alveolar tract and alveoli. This is because the mucus lining from the nasal cavity to the bronchi, bronchioles (especially the larger ones) carries a net negative charge, which tends to entrap positively charged aerosols [25–27]. However, when particles carry a very high net charge, they are prone to being trapped in the upper respiratory tract due to Coulombic interactions with the airway surface. Thus, dependent on particle size and targeted region within the lungs, there exists an optimal range of net charge, typically spanning from several tens to several thousands of elementary charges per particle, that enables particles to bypass the upper airways and effectively deposit in the lower respiratory tract [28,29]. Therefore, a simple and versatile technology that can control both the particle size and surface charge to regulate their deposition in specific regions of the lungs, increase delivery efficiency, minimize exposure to unintended areas, and reduce harmful side effects is desirable [26].

Currently, several technologies are used to generate aerosols for medical applications, such as dry powder inhalers (DPIs), metered-dose inhalers (MDIs), nebulizers, and soft mist inhalers (SMIs) [30]. These devices have different delivery mechanisms, allowing them to adapt to various types of medications. While these technologies can produce particles within the size range suitable for pulmonary drug delivery, they share a common feature: the drug particles must be pre-encapsulated via various methods, such as drug micronization and powder blending, direct controlled crystallization, spray drying, spray freeze drying, particle formation from liquid dispersed systems, and supercritical fluid technologies, before being mixed with the sprayed solution and loaded into the inhalation device [31,32].

Electrohydrodynamic atomization (EHDA) or electrospray (Fig. 1a) has emerged as a superior solution for generating micro/nanosized droplets, particles, and fibers, as well as for the encapsulation of complex therapeutic particles such as core-shell [33–35], multilayer core-shell [36–38], Janus [39,40], porous particles [41–44] and fibers [45–47]. This technique offers precise control over particle size, making it ideal for various applications in different fields, such as biomedical engineering [48,49], pulmonary drug delivery [50], energy and environment [41], and so forth. However, the main drawback of traditional EHDA is that it produces particles with a high surface charge, making

them prone to being attracted to unwanted surfaces during flight [51, 52]. This limitation directly hinders the use of EHDA as a direct drug delivery device for the lungs, as the particles may adhere to the mouth surface rather than reach deeper regions of the lungs. This issue has garnered significant research attention, with various approaches being explored to neutralize the surface charge on particles. For example, the use of a corona discharge needle generates an oppositely charged ionic wind [51,53–57], high-frequency alternating current (AC) atomization is employed to stimulate a resonating meniscus at the orifice [58–60], or low-frequency AC atomization is used to mix oppositely charged particles [50,61–63], thereby neutralizing them. These approaches require multiple independently activated EHDA sources or extremely high frequencies to break the liquid meniscus. This, in turn, demands complex control circuits, which limits the practical application and scalability of the system.

Herein, we propose a bipolar EHDA system as a novel and versatile solution that produces self-neutral particles at high atomization rates, addressing the critical limitation of conventional electrospray technologies on excessive surface charge on aerosolized particles (Fig. 1b). Through both experiments and simulations, the conceptual design, working principle and optimization of the system were demonstrated. The polymeric, drug-loaded polymeric particles were generated with aerodynamic sizes, the charge was optimized for deep lung deposition, and the drug release profile was analyzed. The in vitro deposition efficiency and biocompatibility were also thoroughly evaluated via a lung simulator device, the Andersen cascade impactor system, and cell-based experiments. These findings highlight the strong potential of the bipolar EHDA device for deep lung drug delivery, offering a high deposition rate, a simple operating principle, and biocompatibility.

2. Materials and methods

2.1. Device preparation and atomization analysis

The nozzles used to investigate the bipolar EHDA configuration varied in size, ranging from 22 gauge (22G) to 26 gauge (26G) (Muashi Engineering, Japan), with the specific dimensions of inner diameter, outer diameter, and length provided in Table S3. Two nozzles were connected to 1 ml syringes (Terumo) and secured parallel to each other at a distance d via 3D-printed locking. The solution was dispensed at a constant flow rate via a syringe pump (New Era Pump Systems, Inc.). High-voltage power for the configuration was supplied by a high-voltage pump powered by a closed battery source (EMCO High Voltage Corporation). Taylor cone formation and spraying modes were observed via a digital microscope (Dino-lite EDGE™), whereas particle plumes were recorded via a high-speed camera capable of 4000 fps (Mega Speed) and a microscopic lens (Infinity). All the experiments were conducted in a laboratory environment, with room temperature maintained between 20 and 21 °C and humidity levels between 40 and 70 %. A schematic of the experimental setup is shown in Fig. S1. The solution used for the spraying investigation was 99.5 % isopropyl alcohol (IPA, Sigma-
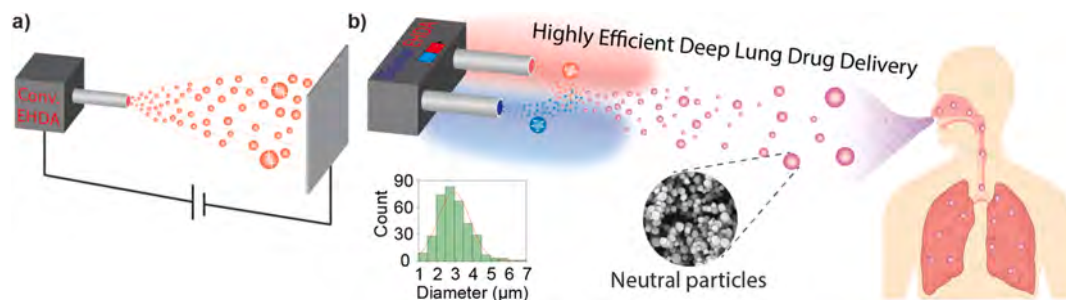
Fig. 1. Concept of pulmonary drug delivery via bipolar EHDA. (a) Conventional EHDA can produce various types of particles, but the high surface charge of these particles limits their direct application for drug delivery. (b) Bipolar EHDA generates neutral particles, enabling direct and efficient drug delivery to the lungs.

Aldrich), with a molecular weight of 60.1 g/mol, a density of 0.785 g/ml, a surface tension of 20.8 mN/m, a viscosity of 1.66 mPas, and a relative permittivity of 17.9.

2.2. Preparation of polymeric, drug-loaded polymeric and dye particles

The Poly(vinylidene fluoride) (PVDF) mixture used in the experiment had a molecular weight of 534,000 g/mol and was in powder form with a density of 1.78 g/cm³. To prepare the sprayed solution, PVDF was dissolved in a mixture of dimethylformamide (DMF, Sigma-Aldrich) and acetone (Sigma-Aldrich) at a 7:3 wt ratio. The solution was stirred overnight at 30 °C via a magnetic stirrer to ensure complete and uniform dissolution of the PVDF. The same process was used for curcumin (Sigma-Aldrich), which is a yellow powder with a molecular weight of 368.38 g/mol. The particles were dyed with Rhodamine B ($\geq$95 %, HPLC, Sigma-Aldrich) with a molecular weight of 479.01 g/mol and a density of 0.79 g/cm³ and with Rhodamine 6G (dye content of ~95 %, Sigma-Aldrich) with a molecular weight of 479.01 g/mol and a density of 1.3 g/cm³.

The solution was sprayed in a closed chamber to eliminate external influences. Particles were collected 10 cm from the nozzles for the analysis of various properties. The particle size and charge were measured via an optical particle sizer (OPS, TSI) and an aerosol electrometer (TSI), respectively. Polymer and drug-loaded polymer particles were collected on a 0.45 μm nylon-6 membrane filter (JVLAB) and then coated with a thin layer of gold for observation under a scanning electron microscope (SEM, Thermo Fisher Scientific) equipped with an energy dispersive spectroscopy (EDS) point and mapping functions for chemical composition analysis. The dyed particles were collected on a 24 × 50 mm cover glass at 10 cm and observed via an FV3000 confocal microscope (Olympus).

2.3. Encapsulation efficiency, loading capacity and drug release preparation

After spraying onto the membrane filter, the drug-loaded particles were weighed to calculate the encapsulation efficiency (EE) and loading capacity (LC) of the system. In this study, two drug loading contents, 1.5 wt% (weight percent) and 3 wt%, were compared, and the polymer concentration was maintained at 3 wt%. To minimize particle dissolution and prevent the release of the encapsulated drug, the residual drug on the filter was quickly washed with 10 ml of ethanol with minimal stirring. The residual drug content was quantified via a filter-based multimode microplate reader (BMG LABTECH) at 428 nm and compared with a calibration curve, and the EE and LC were determined via the following formulas:

$$\text{EE (\%)} = \frac{\text{Weight of drug in particles}}{\text{Weight of drug in solution}} \times 100\% \tag{1}$$

$$\text{LC (\%)} = \frac{\text{Weight of drug in particles}}{\text{Weight of drug + polymer in solution}} \times 100\% \tag{2}$$

To evaluate the controlled drug release capability, the membrane filter, after being washed to remove residual drug, was placed into a dialysis membrane with a molecular weight cutoff (MWCO) of 3.5 kDa (Sigma-Aldrich). The membrane was then immersed in a container containing 20 ml of phosphate buffered saline (PBS) containing 0.5 wt% polysorbate 20 (Sigma-Aldrich), which acts as a surfactant to increase the solubility of curcumin (CUR) during the release process. At predefined time points, 1 ml of the supernatant was withdrawn and transferred into designated Eppendorf tubes, while 1 ml of fresh medium was added to the container to maintain the release conditions. The amount of curcumin released at each time point was determined via a calibration curve, and the release profile was plotted based on the equation provided below.

$$\text{Cumulative release (\%)} = \sum_0^t M_t \Big/ M_0 \times 100\% \tag{3}$$

where M_t is the drug released at time point t and M_0 is the amount of curcumin loaded in the particles.

2.4. Andersen cascade impactor

The Anderson Cascade Impactor (ACI) (Copley, United Kingdom) was placed in a refrigerator at 5 °C for 90 min to ensure that the internal environment of the ACI reached 100 % relative humidity [64]. The ACI was then connected to a vacuum pump set at a flow rate of 28.3 L/min, which is the standard flow rate used in experiments with the ACI for evaluating the metered-dose inhalers (MDIs) and is widely employed in assessing particle size distributions [65]. The experimental setup is shown in Fig. 6b. After being sprayed for 10 min, each stage plate was rinsed with 15 ml of ethanol, and the collected solution was then analyzed using a UV-1800 spectrophotometer (Shimadzu) to quantify the amount of curcumin deposited on the plate. From the mass values obtained and the cutoff diameter (Table S4) at each stage, the mass median aerodynamic diameter (MMAD), geometric standard deviation (GSD), and fine particle fraction (FPF) were calculated via formulas based on ISO 27427:2013 - Anaesthetic and respiratory equipment - Nebulizing systems and components [66,67].

2.5. Cell treatment

RAW264.7 cells were cultured on 12 mm sterile glass coverslips placed in a 24-well plate at a density of 3 × 10⁴ cells per well for adherence. The plate was incubated at 37 °C in a 5 % CO₂ incubator. Coverslips containing cells were removed from the culture medium, positioned on the stage with the highest weight of curcumin in the ACI test (stage 4), and then sprayed for different durations - 2 min, 3 min, and 5 min. An equivalent number of coverslips were removed from the culture medium for the same duration without exposure to spray and were used as the control group. After spraying, the coverslips were returned to the culture medium and incubated for 24 h in Dulbecco's modified Eagle's medium (DMEM) supplemented with 10 % fetal bovine serum (FBS). After 24 h, two assays were performed to assess cell viability.

Live/dead cell staining: Cells were incubated with a staining solution containing Calcein-AM (Thermo Fisher) and propidium iodide (PI) (Thermo Fisher), with final concentrations of 2 μM and 1 μg/ml, respectively, for 30 min at 37 °C in the dark. After staining, the cells were washed gently with PBS and observed under a confocal microscope. Live cells appeared green (calcein-AM), and dead cells appeared red (PI).

For the Cell Counting Kit-8 (CCK-8) assay, 10 μL of CCK-8 (Dojindo, Japan) solution containing 200 μL of fresh culture medium was added directly to each well, ensuring uniform mixing without disturbing the cells, followed by incubation at 37 °C for s1 h. The plate was protected from light during incubation to maintain reagent stability. After incubation, the absorbance at 450 nm was measured via a filter-based multimode microplate reader (BMG LABTECH).

SEM samples were prepared as follows: immediately after treatment and after 24 h of incubation, the cells on coverslips in 24-well plates were fixed with 200 μL of 4 % paraformaldehyde (PFA) per well. Fixation was carried out at room temperature for 15 min. After fixation, the PFA solution was removed, and the cells were washed three times with PBS to remove any residual fixative. Then, the coverslips were coated and used for evaluation via SEM.

2.6. Statistical analysis

All measured values are presented as mean ± standard deviation.

Statistical analysis and plots were performed using Microsoft Excel.

## 3. Results and discussion

3.1. Working principle

The concept of the bipolar EHDA system is grounded in the principle that the mixing of oppositely charged particles, facilitated by ion winds from opposite pole nozzles, can lead to the generation of neutral particles [50,53,68]. In this new design, the two nozzles play equivalent roles, functioning as particle atomizers and neutralizers for the particles emitted by the opposite nozzle. As shown in Fig. 2a, the two nozzles are arranged parallel with a separation distance of d = 12 mm. The nozzles are connected to the positive and ground terminals of a closed battery source, ensuring that the current is balanced between the nozzles following Kirchhoff's law of charge conservation [69].

With this setup, when the floating voltage is applied to the nozzles, an electric field is generated, which is directed from the positive nozzle to the ground nozzle. The electric charge is most concentrated at the tip of each nozzle, particularly at the edges. When the charge density becomes sufficiently high, ionization can occur in the surrounding air, forming a cloud of charged particles. Thus, each nozzle not only generates charged droplets but also produces charged clouds, commonly referred to as ion winds, which are associated with atomization [53,69, 70]. Within the liquid at the nozzles, the electrostatic force generated by the electric field increases until it overcomes the surface tension of the liquid, causing the liquid to deform into a Taylor cone. When the electrostatic force surpasses the liquid's surface tension, the liquid surface disintegrates, emitting a plume of smaller, charged droplets [71].

According to the fundamental principles of charged particle motion in an electric field, droplets emitted from the positively charged nozzle move in the direction of the electric field due to the electrostatic force (F_e), whereas negatively charged droplets emitted from the ground nozzle move in the opposite direction. As the particles from the two nozzles approach each other, the contributions of each particle charge and the oppositely charged ion clouds to the electric field result in a localized electrostatic force (Coulomb force (Fc)) between oppositely charged droplets. This interaction leads to instant charge neutralization, allowing the neutralized particles to move away from the nozzles as the forces reach equilibrium. This is illustrated in Fig. 2a, where the neutral particles move in the direction of the velocity vector $\vec{v}$.

A computational fluid dynamics (CFD) model was developed via the open-source software OpenFOAM to demonstrate the formation of Taylor cones and the movement of particles under the influence of an electric field. The simulation employs Taylor - Melcher's leaky-dielectric model, providing a system of governing equations to consider the fluid-dynamic and electrostatic regimes involved in atomization [72–74]. The details of the governing equations, simulation domain, meshing and configuration parameters are presented in Section S1 of the supplementary information.

Fig. 2b shows the simulation results of Taylor cone formation and the mutual attraction of particles generated from the two nozzles. This result is validated by the experiment shown in Fig. 2d, where isopropyl alcohol (IPA) solution is sprayed at a flow rate of 1 ml/h from each nozzle. Each nozzle creates a Taylor cone, and the sprayed plumes merge as they exit the nozzles, neutralize each other, escape the electric field, and continue moving forward. Fig. 2c provides a more detailed analysis of the process, showing how particles from the two nozzles attract each other, interact,
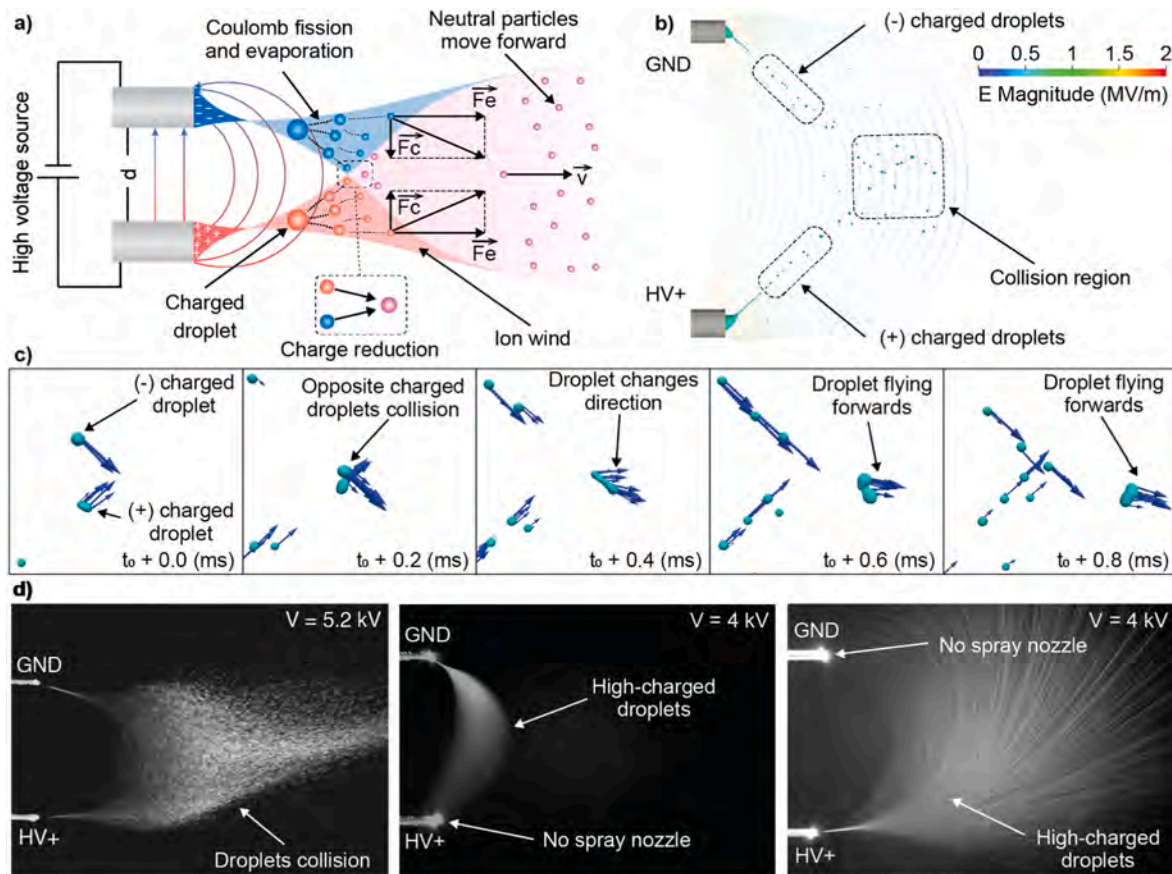
Fig. 2. Concept of bipolar EHDA. (a) Working principle of bipolar EHDA, where charge reduction is achieved by mixing oppositely charged particles and ion wind. (b) Simulation showing two sprayed plumes attracting, colliding, and neutralizing each other. (c) Enlarging the collision area in Figure b, illustrating how the oppositely charged droplets change their directions over time. (d) Atomization behavior under three regimes: both sides are sprayed, and only one side is sprayed.

and change their velocity vectors over time. After the droplets collide, they alter direction and move forward. The spraying process has to occur simultaneously at both nozzles, as without the presence of particles from the opposing nozzle, the particles cannot be neutralized and will be trapped within the electric field and will fly toward the nonspraying nozzle (Fig. 2d).

3.2. Spray stability of bipolar EHDA

The stability of the bipolar EHDA configuration was evaluated by spraying IPA while varying the applied voltage and flow rate. IPA is a pure liquid with low surface tension, which was employed instead of a surfactant solution, aiming to avoid surface tension gradients that arise from the uneven distribution of surfactant molecules under a concentrated electric field [50]. The applied voltage was adjusted to determine the threshold for stable dual cone jet mode and avoid instabilities such as multijet or dripping modes. Additionally, the flow rate was adjusted to examine its influence on the balance between electrostatic forces and the liquid surface tension, aiming for stable atomization.

From the experiments, we observed that for nozzles of the same size, the nozzle connected to the positive electrode requires a lower voltage to maintain a Taylor cone than the nozzle connected to the ground electrode does, as shown in Fig. 3b, for the 26-gauge nozzle pairs. This finding aligns with the conclusion of the study by H.H. Kim et al. [75], which stated that corona discharge is weaker at negative polarity. Consequently, the electrostatic force at the ground-connected nozzle is weaker under the same voltage conditions as the positively charged nozzle.

To identify the stability region between the two nozzles, we refer to the theoretical onset voltage for the atomizing process [76], using the following formula $V_0 = \sqrt{\gamma R_0/\varepsilon_0} \ln(4d/R_0)$, where γ is the surface tension, R_0 is the outer radius of the nozzle, ε_0 is the relative permittivity, and d is the distance between the two nozzles. Therefore, when the nozzle diameter decreases, the threshold voltage for atomizing decreases. Consequently, to achieve equilibrium, the diameter of the negative nozzle should be smaller than that of the positive nozzle to optimize this balance region.

Fig. 3 provides information about the stability of the bipolar EHDA design for each nozzle when the flow rate and applied voltage across different nozzle pairs are varied. In these experiments, a 26G nozzle was connected to the ground electrode, while the positive electrode varied from 26G to 22G. For each nozzle pair, the source voltage varied from 0 to 7 kV, and the flow rates at both nozzles were simultaneously adjusted from 0.3 to 1.5 ml/h (corresponding to a total flow rate of 0.6–3 ml/h). This flow rate range was selected because it corresponds to the operating conditions typically required by conventional electrospray systems to produce fine, monodisperse micro- and nanoparticles, especially in bioengineering applications [77,78].

Fig. 3a illustrates the changes in spray mode for the 22G–26G nozzle pair. When the voltage is within the range of 4–5 kV, the nozzle connected to the positive electrode maintains a stable single-jet mode, whereas the nozzle connected to the ground electrode achieves this mode only when the applied voltage exceeds 5 kV. In the voltage range of 5–5.5 kV, the highlighted region represents the stable operating conditions targeted in this study, where both nozzles maintain single-jet mode. During this phase, the two sprayed plumes attract each other, neutralize their charges, and maintain their forward momentum. However, as the voltage increases beyond 5.5 kV, the positive electrode nozzle is sprayed earlier and transitions into multijet mode. The ground electrode nozzle follows and transitions to multijet mode when the voltage exceeds 6 kV. The changes in the flow rate along the horizontal axis indicate that higher flow rates require only a slightly higher voltage to maintain the same spray mode.

Similar adjustments were made for other nozzle pairs, as shown in Fig. 3b. For the nozzle pairs 23G-26G and 24G-26G, the stable range was similar to that of the G22-G26 pair, whereas this range became narrower as the nozzle sizes became more identical in the pairs G25-G26 and G26-G26. For some flow rates in these nozzle pairs, stability could not be achieved at either nozzle, such as 23G-26G at 1.8 ml/h or 25G-26G at 1.4 ml/h, because the voltage required for the ground nozzle to reach single-jet mode exceeded the voltage, causing the positive nozzle to enter multijet mode. This instability is attributed to the open-space experimental setup, where the temperature and humidity conditions varied.

These findings clearly indicate that achieving stable operation at both nozzles is feasible for the tested pairs. However, the stability range is broader and easier to maintain when the ground nozzle is smaller than the positive nozzle. This conclusion aligns well with theoretical predictions based on the onset voltage equation. Among the tested nozzle pairs, the 24G-26G pair exhibited the largest stability region, indicating
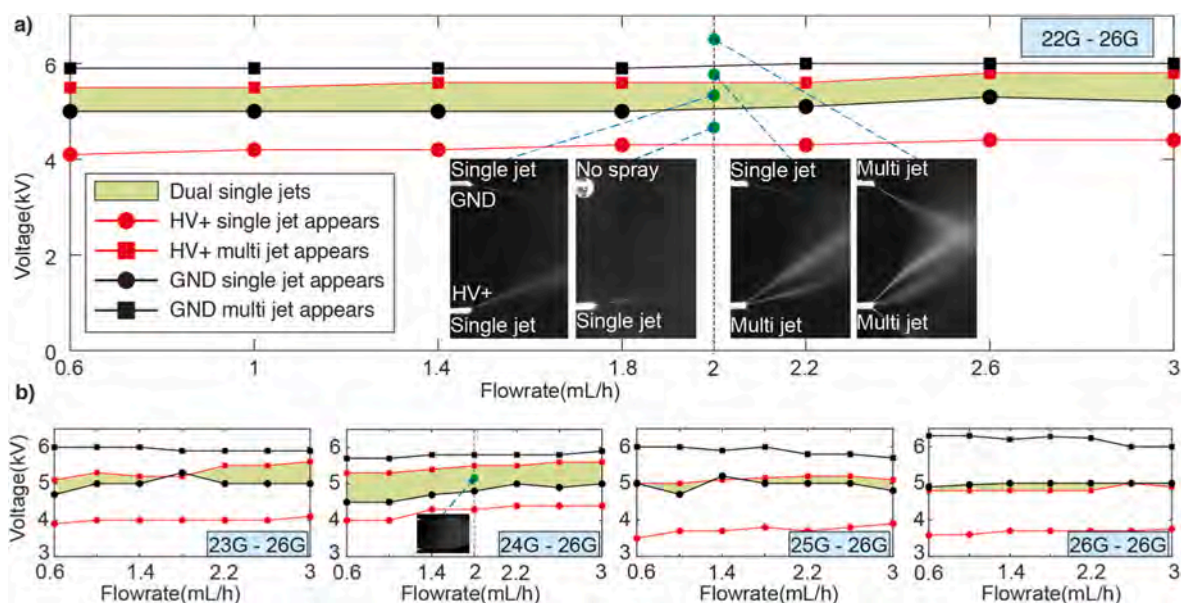

Fig. 3. Atomization optimization by varying the nozzle size and flow rate. The green areas indicate conditions where both nozzles operate in single-jet mode. (a) 22G and 24G nozzles are connected to the positive and ground electrodes. (b) The positive side is alternately tested with 23G, 24G, 25G or 26G nozzles.

its superior performance in maintaining stable spraying conditions. Beyond spray stability, the 24G–26G nozzle pair falls within a range of nozzle sizes that was selected for investigation due to proven suitability in biomedical applications. Nozzles within this size range have demonstrated the ability to maintain stable operation and consistently generate micro- and nanoparticles, which is critical for deep lung deposition and various other biomedical applications [50,79]. Consequently, this nozzle pair will be utilized for further investigations.
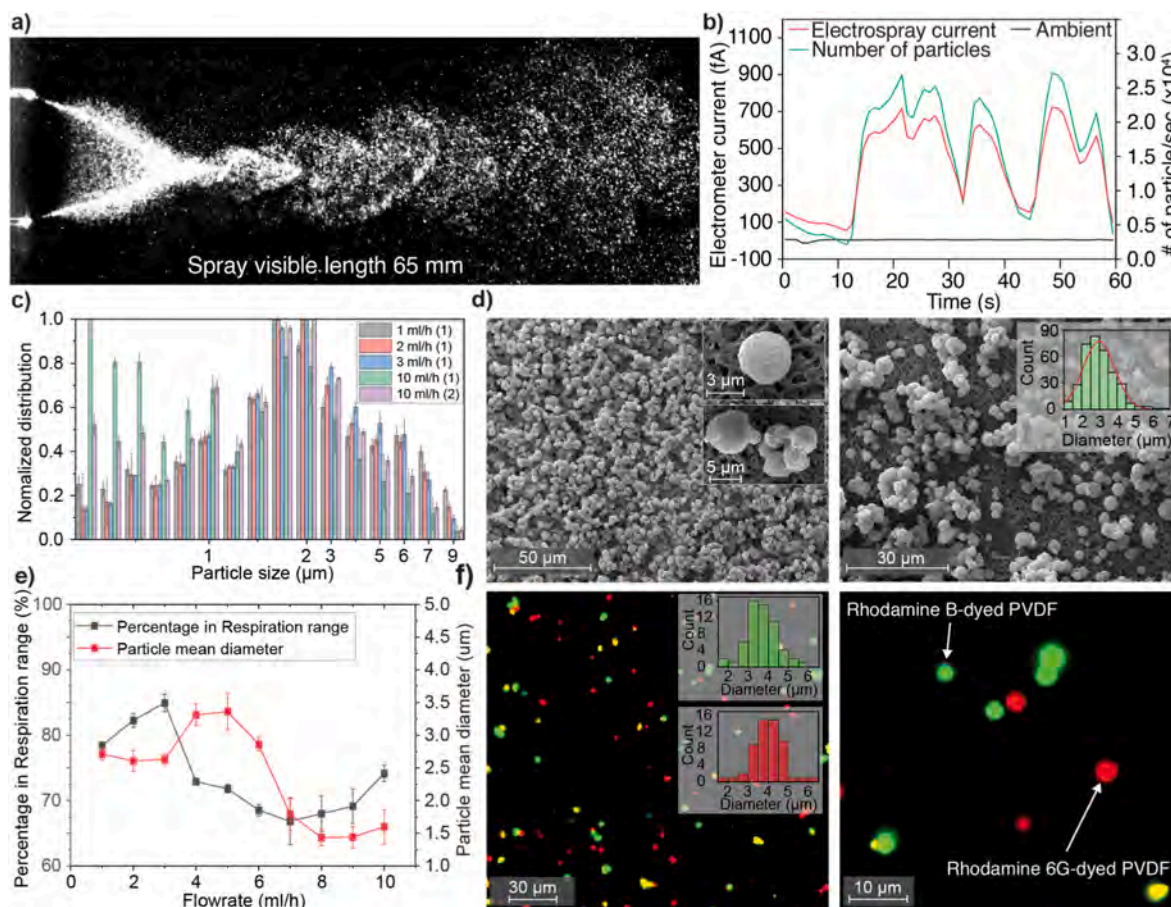
3.3. Polymeric particles

The characteristics of bipolar EHDA demonstrate its significant potential in biomedical applications such as drug delivery into cells or loading drugs into the lungs. To explore and substantiate the promise in these applications, we opted to atomize the polymer particles and analyze their resulting properties. Polyvinylidene fluoride (PVDF) was selected as the material for the sprayed polymer particles because of its well-established biocompatibility and widespread use in cell culture applications [80]. PVDF (5 wt%) was dissolved in DMF and acetone at a 7:3 ratio.

Fig. 4a illustrates the atomization generated from both nozzles using 5 wt% PVDF with DMF and acetone as solvents. The video capture of the bipolar EHDA generating PVDF particles can be found in movie S1. To demonstrate that the polymeric particles generated by the bipolar EHDA system were effectively neutralized, we used an electrometer (TSI) to measure the particle charge at various positions. The particle count reached tens of thousands per second, and the total charge of the particles represented by the electrometer current is shown in Fig. 4b. Near the positive and negative nozzles, the particle charge exceeded ±1 pA (the upper and lower detection limits of the electrometer). However, measurements taken in the middle of the plume revealed that the total electrometer current was reduced to only a few hundred femtoamperes. Average calculations revealed that the number of elementary charges per particle was approximately 166, corresponding to a surface charge density of 7.5×10^{-6} charges/nm^2 after neutralization by the bipolar EHDA system. This represents the optimal charge per particle for effective deposition in the deep lung regions, particularly within the bronchioles and alveoli, where the airway radius is small and airflow velocity is low. Under these conditions, electrostatic interactions between charged particles and the epithelial surfaces become the dominant deposition mechanism, surpassing other mechanisms such as inertial impaction, gravitational sedimentation, and Brownian diffusion [28,29].

Fig. 4c shows the results of the particle size measurements when the samples were sprayed at various flow rates via an optical particle sizer (OPS). At lower flow rates of 1, 2, and 3 ml/h, the polymer particles produced were relatively uniform, with most particles measuring between 1 and 5 μm and an average diameter of 2.65 μm. When the flow rate increases significantly to 10 ml/h and the applied voltage is increased to maintain the cone-jet mode, the particles become less uniform, with most having sizes below 1 μm (Fig. S3). This occurs because, as the voltage increases, the charge on each droplet at the first atomization step also increases, causing further droplet breakup into smaller particles during flight [81,82]. With a slight adjustment to the

Fig. 4. Generation of polymeric particles via bipolar EHDA. (a) A 5 wt% PVDF sprayed plume captured by a high-speed camera. (b) Electrometer current measurements of the atomization. (c) Optical particle size (OPS) data at different flow rates; pair (1) uses nozzles G24-G26, whereas pair (2) uses nozzles G20-G24. (d) SEM images of 5 wt% PVDF particles with a spray flow rate of 1 ml/h; most of the particles are in the respiratory range. (e) Mean particle diameter and percentage within the respirable range across different flow rates in the case of the G24-G26 nozzle pair. (f) Confocal microscopy images comparing PVDF particles with and without dye from the two nozzles. The green and red colors represent Rhodamine B-dyed PVDF and Rhodamine 6G-dyed PVDF particles, respectively.

nozzle size using the larger nozzle pair (20G-24G) to decrease the flow velocity and prevent larger droplets in the first atomization step, our system successfully sprayed at 10 ml/h, producing relatively uniform particles similar to those achieved at lower flow rates with the previous nozzle pair. This is one of the highest flow rates ever achieved in polymer generation by atomization, where the particles remain small, averaging a few micrometers, and exhibit uniformity [51,83,84]. The flow rate is close to the basic requirements for a medical nebulizer [85–87]. A detailed comparison can be found in Table S5. These measurements were confirmed by the SEM images shown in Fig. 4d, which indicate uniform particle sizes, with most particles falling within the optimized target size range. The consistency between both measurement methods demonstrates that the spraying process reliably produces particles of the desired size, which are suitable for pulmonary drug delivery applications.

Furthermore, the investigation across different flow rates (Fig. 4e) indicates that most particles fall within the respiration range of approximately 65 %–85 %, with the optimal flow rate being 3 ml/h. As the flow rate increases, the mean diameter remains within the respiration range but tends to decrease slightly. Therefore, by adjusting various flow rates and switching to larger nozzles at higher flow rates, the results confirm that the bipolar EHDA configuration is highly versatile and can easily achieve the desired particle size even at very high flow rates.

To evaluate the size uniformity of the particles generated from both nozzles, an experiment was conducted using dyed particles from each nozzle. The solution was sprayed at a flow rate of 1 ml/h for each nozzle, and the particles were collected on a cover slip and observed under a confocal microscope. For the positive nozzle, a solution of 5 wt% PVDF and 0.1 wt% Rhodamine B in DMF and acetone was used. Similarly, the ground nozzle was loaded with the same PVDF solution, but 0.1 wt%

rhodamine 6G was used as the dye. Fig. 4f indicates that the particles from both nozzles have similar sizes, with most particles having diameters between 3 and 5 μm. This demonstrates that, despite the two nozzles having different diameters, they experience equal electrostatic forces when connected to the same battery power source.

3.4. Curcumin-loaded polymeric particles

Based on the measurement and observation results from atomizing the PVDF polymer, we further demonstrated the feasibility of drug delivery by conducting an experiment in which PVDF was combined with curcumin (CUR). The objective was to assess whether the bipolar EHDA system could effectively generate polymer-drug particles while maintaining particles in the respiratory range and ensuring proper drug encapsulation. Curcumin, a yellow compound extracted from the *Curcuma longa* plant, was chosen for this experiment because it has been used in traditional medicine because of its anti-inflammatory, antiseptic, and analgesic activities [88,89] and its potential applications in treating lung diseases, such as asthma, pulmonary fibrosis, COPD, and lung cancer [90]. The encapsulation of CUR in polymers via the atomization technique offers a promising approach to overcome the limitations of CUR in practical clinical trials, such as its poor solubility in aqueous solvents, which leads to reduced bioavailability [91,92]. Furthermore, curcumin's chemical stability and strong chromophoric properties allow for straightforward quantification during processing and release studies [93,94].

Fig. 5a and the measurement results from the electrometer in Fig. 5b show that the PVDF@CUR3 particles freely travel forward over a long distance, demonstrating that the particles were successfully neutralized through the bipolar EHDA configuration. The current measured by the
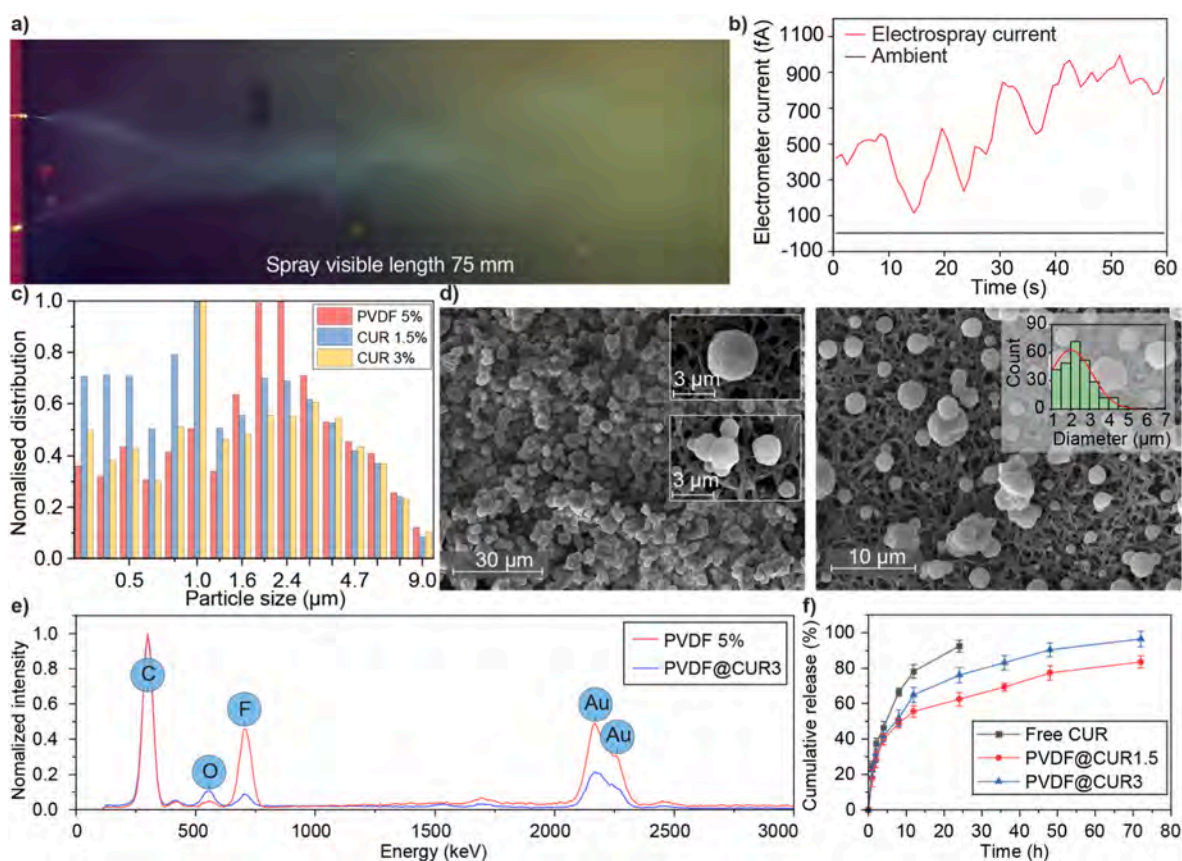
Fig. 5. Generation of drug-loaded polymeric particles. (a) A PVDF 3 % - CUR 3 % (PVDF@CUR3) sprayed plume captured by a phone camera. (b) Electrometer current measurements of PVDF@CUR3 atomization. (c) Comparison of OPS data for three cases: 5 wt% PVDF only, PVDF 3 % - CUR 1.5 % (PVDF@CUR1.5), and PVDF@CUR3. (d) SEM images of PVDF@CUR3. (e) EDS spectra of two samples: 5 wt% PVDF only and PVDF@CUR3.
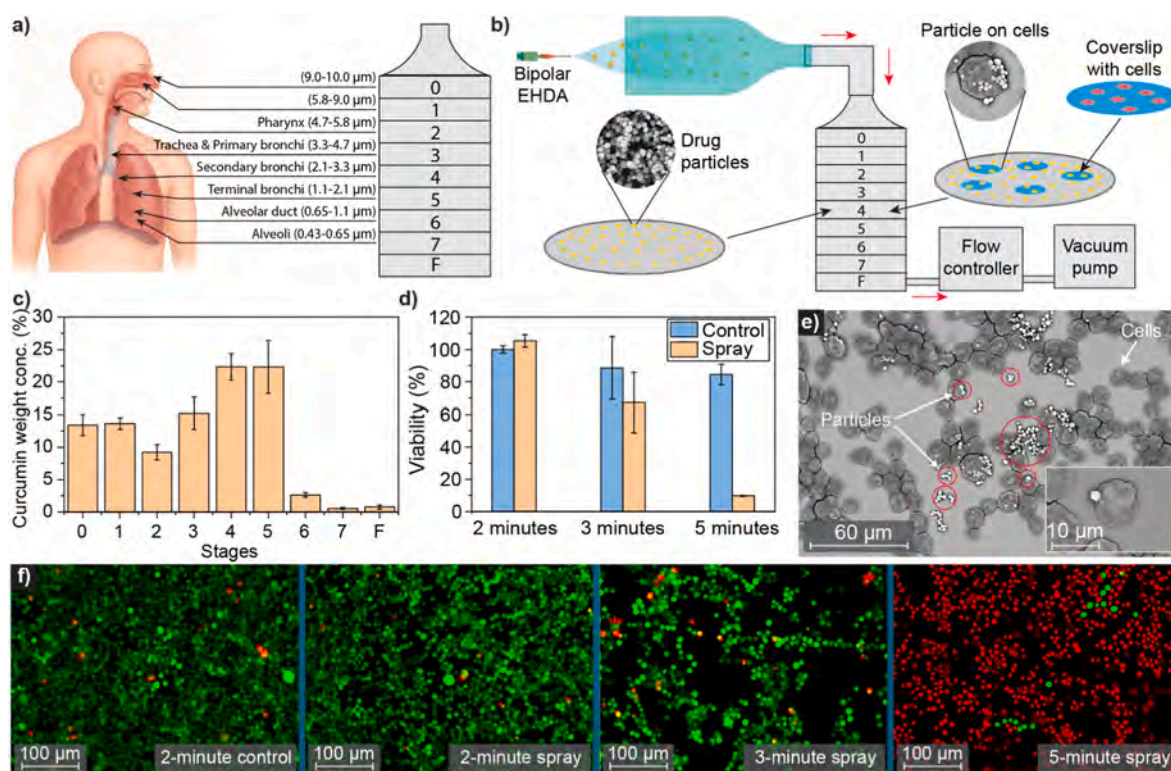
Fig. 6. Particle deposition with ACI and cell cytotoxicity test results. (a) The stages of ACI correspond to the levels of the respiratory tract [104]. (b) Experimental setup of the deposition test and the cell test. (c) Weight concentration of curcumin at various stages of ACI. (d) Cell viability at stage 4 of the ACI after different spray durations. (e) SEM image of particles deposited on the cells. (f) Confocal microscope images of the control cells and different spray durations.

electrometer also falls within the range of a few hundred femtoamperes, further confirming the effective neutralization of the particles. The video capture of the bipolar EHDA generating PVDF particles can be found in movie S2.

Two mixtures, PVDF 3 % - CUR 1.5 % (PVDF@CUR1.5) and PVDF 3 % - CUR 3 % (PVDF@CUR3), were sprayed via the bipolar EHDA configuration at a flow rate of 1 ml/h for each nozzle. The particles collected by OPS, as shown in Fig. 5c, predominantly range in size from a few hundred nanometers to 5 μm. However, the number of particles smaller than 1 μm was significantly greater than that in the PVDF 5 % case because of changes in the physical properties of the solution with the addition of CUR. In the PVDF@CUR1.5 case, the number of sub 1 μm particles is greater than that in the PVDF@CUR3 case, likely due to the reduction in conductivity with increasing CUR concentration [95,96]. These measurement results are consistent with the SEM images in Fig. 5d, which show a substantial number of small particles in the sub 1 μm range. These results further affirm that the bipolar EHDA configuration is highly suitable for delivering drugs into the lungs, as it consistently produces polymeric-organic particles within the optimal size range for pulmonary drug delivery.

To confirm the presence of both PVDF and CUR in the particles, SEM-EDS (energy-dispersive spectroscopy) was used to analyze the chemical composition of the particles. In Fig. 5e, the red line indicates that the intensity of the fluoride peak is significantly greater than that of the oxygen peak, which is consistent with the chemical structure of PVDF, which does not contain oxygen $(C_2H_2F_2)_n$. Although the EDS spectrum still shows an oxygen peak, this peak can be attributed to the use of a Nylon 6 membrane filter for particle collection, which has an atomic structure $(C_6H_{11}NO)_n$. In contrast, curcumin (CUR) contains oxygen in its molecular structure $(C_{21}H_{20}O_6)$, and as a result, the EDS spectrum of the PVDF@CUR3 particles (blue line) shows an oxygen signal comparable in intensity to the fluoride peak. This comparison further confirmed the successful encapsulation of curcumin within the PVDF particles.

3.5. Encapsulation efficiency (EE), loading capacity (LC), and drug release

Two formulations, PVDF@CUR1.5 and PVDF@CUR3, were examined to evaluate their drug loading and release capabilities, with the aim of exploring the controlled release potential of CUR-loaded PVDF particles. The encapsulation efficiency (EE) and loading capacity (LC) were initially identified as essential metrics to assess the CUR encapsulation performance of the PVDF carrier. The EE values for PVDF@CUR1.5 and PVDF@CUR3 showed minimal differences, with values of 62.0 ± 2.5 % and 65.4 ± 2.3 %, respectively. However, the LC of PVDF@CUR3 was notably greater, reaching 35.5 ± 1.1 %, than the 22.6 ± 1.9 % for PVDF@CUR1.5. These results suggest that increasing the drug-to-polymer ratio enhances the drug-loading capacity but does not affect the encapsulation efficiency, indicating that a higher drug input does not necessarily yield proportional benefits.

The release profiles are shown in Fig. 5f. Compared with the control sample, neither the PVDF@CUR1.5 nor the PVDF@CUR3 sample exhibited significant burst release. The control formulation displayed rapid drug release, reaching 92.5 ± 3.3 % after 24 h. In contrast, the PVDF@CUR1.5 formulation resulted in a slower release rate, reaching 83.5 ± 3.5 % after 72 h, whereas the PVDF@CUR3 formulation resulted in a faster release rate, reaching 96.5 ± 4.3 % at the end of the evaluation. This difference can be attributed to differences in the drug-loading capacities between the two formulations, which results in varying drug concentration gradients between the carrier interior and the surrounding medium, accelerating the release process in the PVDF@CUR3 formulation compared with that in the PVDF@CUR1.5 formulation.

To substantiate this observation, the release profiles were analyzed via kinetic models. Both formulations strongly correlated with the Higuchi and Korsmeyer–Peppas models (Fig. S4 and S5). The Higuchi

model suggests that drug release is predominantly governed by diffusion, which is consistent with the behavior of drug particles dispersed in a solid matrix [97–99]. Moreover, the release exponent n from the Korsmeyer–Peppas model provides insights into the release mechanism [100,101]. The n values for PVDF@CUR1.5 and PVDF@CUR3 were 0.4463 and 0.4003, respectively. These values indicate an anomalous (non-Fickian) transport mechanism, where both diffusion and erosion contribute to drug release, as detailed in Table S6.

3.6. Lung model with the Andersen cascade impactor (ACI)

The cascade impactor is the most widely used instrument for in vitro determination of aerosol particle size distribution from medical nebulizers [102,103]. It consists of 8 stages, numbered from 0 to 7, each corresponding to a specific region of the human respiratory tract, ranging from the nasal cavity to the alveoli. Each stage has a distinct cutoff diameter, which represents the aerodynamic particle size capable of depositing at that stage, as illustrated in Fig. 6a [104]. This device enables direct assessment of the mass mean aerodynamic diameter (MMAD), a key parameter that characterizes particle transport within the respiratory tract. Additionally, it allows evaluation of particle size uniformity through the geometric standard deviation (GSD) and quantification of the fine particle fraction (FPF) (aerodynamic diameter <5 μm) [105,106]. In this experiment, PVDF@CUR1.5 was delivered through the bipolar EHDA device into the ACI, as shown in Fig. 6b, to evaluate the particle deposition efficiency within a lung model. Details of the experiment are provided in the Materials and Methods section.

Fig. 6c shows that particle deposition primarily occurred from stages 0–5, corresponding to regions of the respiratory tract extending from the nasal cavity to the terminal bronchi. In contrast, significantly lower deposition was observed at stages 6 and 7 and in the final filter, which represents the alveolar ducts and alveoli [107]. The highest amounts of curcumin were detected at stages 4 and 5, corresponding to the secondary and terminal bronchi, respectively. These results indicate that the bipolar EHDA system is particularly well suited for treating diseases that predominantly affect these regions, such as chronic obstructive pulmonary disease (COPD), asthma, bronchitis, and bronchiectasis [108,109].

On the basis of the measured mass of curcumin deposited across the stages of the ACI, the deposition efficiency, MMAD, GSD, and FPF are summarized in Table S7 alongside results from other studies. The curcumin delivery efficiency into the ACI reached 80.8 %, demonstrating excellent performance compared with many other drug delivery devices tested under similar conditions, including MDIs at 33.3 %–74 % [110], jet nebulizers at 2.3 %–10 %, vibrating mesh nebulizers at 3.9 %, and DPIs at 1.5 % [111–113]. Moreover, the MMAD and GSD values of 2.18 ± 0.17 μm and 2.66 ± 0.24, respectively, indicate that the bipolar EHDA system effectively generates drug particles within the optimal aerodynamic size range for the inhalation system [107]. Although the GSD of 2.66 reflects a relatively broad particle size distribution, it remains well within the acceptable threshold for pulmonary drug delivery systems [114,115]. The high FPF value of 72.98 ± 0.83 % further supports the superior performance of the device in delivering a substantial fraction of the drug to deep lung regions.

3.7. In vitro cytotoxicity

In clinical applications, assessing potential toxicity is critically important, particularly for pulmonary drug delivery. Macrophages are commonly used in toxicity studies because they serve as the first line of defense and are the primary cells that recognize foreign substances, such as drugs, introduced into the body [116]. RAW264.7 cells are a mouse macrophage-like cell line that has functions similar to those of primary macrophages. They are commonly used as models for tumor-associated macrophages in research [117–119]. To demonstrate the biosafety of the PVDF@CUR particles generated from our platform, RAW264.7 cells

were cultured on 12 mm glass coverslips, which were then placed on stage 4 of the Andersen Cascade Impactor - the stage with the highest drug deposition in the ACI test and exposed to the spray for 3 durations: 2, 3, and 5 min, corresponding to approximately 5.75, 8.62, and 14.73 μg of curcumin deposited per coverslip, respectively, as shown in Fig. 6b.

Fig. 6e confirms that these particles effectively deposit on the cell surface, demonstrating that the direct spraying method onto cells placed within the ACI can be reliably used to evaluate particle–cell interactions and assess the biological effects of drug-loaded particles. The CCK-8 results shown in Fig. 6d indicate that after 2 min of exposure, the PVDF@CUR1.5 particles did not exhibit any cytotoxic effects on the cells. As the exposure time increased, a clear trend emerged in which cell viability decreased in both the sprayed and control groups. The percentage of viable cells decreased to 68 % at 3 min and further decreased to 9.8 % at 5 min. These observations were further supported by confocal microscopy images (Fig. 6f), which revealed that the 2-min control and spray groups presented similar cell viabilities, whereas the 3-min spray group presented a noticeably greater ratio of dead to live cells. In the 5-min spray group, most of the cells were no longer viable, with only a few remaining alive.

These findings are consistent with those of previous studies on the effects of curcumin on RAW264.7 cells, which reported that curcumin is safe and nontoxic at low concentrations but can become cytotoxic at higher doses [120,121]. Additionally, the control samples also showed reduced viability over longer durations outside the culture medium, suggesting that extended environmental exposure alone can contribute to cell death. These results confirm that the PVDF@CUR particles generated by the bipolar EHDA device exhibit biocompatible properties under appropriate dosage and exposure conditions, as the ratio of viable cells in the spray samples to that in the control samples exceeded 70 %, in accordance with ISO 10993–5:2009 standards [122].

4. Conclusions

In this study, we presented a novel and simple bipolar EHDA device through both experimental and simulation approaches. The validation results revealed that the particles and ion winds generated from the two oppositely charged nozzles attracted and neutralized each other, allowing the self-neutral particles to continue forward momentum. The experiments demonstrated the system's effectiveness in producing micro/nanosized droplets and particles that are electrically neutralized. The device is capable of atomizing in different modes and is influenced primarily by voltage adjustments and nozzle size, whereas the flow rate has a minimal effect on spray stability.

The bipolar EHDA device has been shown to successfully spray polymer and polymer-organic particles of micro/nano sizes. The particle sizes ranged from a few hundred nanometers to under 10 μm, mostly within the range suitable for pulmonary inhalation, and the residual charge on each particle was reduced to just a few hundred charges per particle, even at 10 ml/h, enabling efficient deposition in the deep lung. Moreover, the deposition test using the ACI demonstrated that the device effectively produces particles with low aerodynamic diameters, and a majority of these particles are capable of depositing within the deep lung region, with the highest deposition observed in stages 4 and 5, corresponding to the secondary and terminal bronchi.

Drug delivery efficiency evaluation further indicated that the bipolar EHDA system is capable of encapsulating drugs effectively, with high loading capacity and slow release times, making it suitable for various therapeutic applications. The cytotoxicity results demonstrate that the drug particles exhibit good biocompatibility and are safe for pulmonary drug delivery when administered within appropriate concentration ranges.

Overall, the bipolar EHDA device is a highly promising technique for pulmonary drug delivery, offering a controlled, efficient, and scalable method for delivering therapeutic agents directly into the lungs. This

method holds significant potential for advancing the field of pulmonary drug delivery, optimizing treatment efficacy, and improving patient outcomes. In the future, magnetic particles and drugs with optically adjustable release rates, as well as more complex particle structures, could be integrated into bipolar EHDA devices. This highlights the broad potential of bipolar EHDA not only in drug delivery and healthcare but also in fields such as chemistry, agriculture, and environmental applications**.**

CRediT authorship contribution statement

Van Canh Doan: Writing – original draft, Visualization, Methodology, Investigation, Formal analysis, Data curation, Conceptualization. **Ngoc Luan Mai:** Investigation, Formal analysis. **Cuong Hung Luu:** Investigation, Formal analysis. **Donglin Cai:** Investigation, Formal analysis. **Wendong Gao:** Investigation, Formal analysis, Conceptualization. **Trung Hieu Vu:** Visualization, Investigation. **Hoai Duc Vu:** Visualization, Investigation. **Thi Van Anh Hoang:** Visualization, Investigation. **Duc Khanh Tran:** Visualization, Investigation. **Dzung Dao:** Writing – review & editing, Conceptualization. **Hang Thu Ta:** Resources, Conceptualization. **Yin Xiao:** Resources, Conceptualization. **Peter Woodfield:** Writing – review & editing, Writing – original draft, Supervision. **Van Thanh Dau:** Writing – review & editing, Writing – original draft, Supervision, Project administration, Methodology, Funding acquisition, Conceptualization.

Declaration of competing interest

The authors declare that they have no known competing financial interests or personal relationships that could have appeared to influence the work reported in this paper.

Acknowledgments

Appendix A. Supplementary data

Supplementary data to this article can be found online at https://doi.org/10.1016/j.mtadv.2025.100626.

Data availability

Data will be made available on request.

References

[1] A.B. Karbasi, J.D. Barfuss, T.C. Morgan, D. Collins, D.A. Costenbader, D. G. Dennis, A. Hinman, K. Ko, C. Messina, K.C. Nguyen, Sol-moiety: discovery of a water-soluble prodrug technology for enhanced oral bioavailability of insoluble therapeutics, Nat. Commun. 15 (1) (2024) 8487, https://doi.org/10.1038/s41467-024-52793-6.

[2] K. Gou, Y. Wang, X. Guo, Y. Wang, Y. Bian, H. Zhao, Y. Guo, Y. Pang, L. Xie, S. Li, Carboxyl-functionalized mesoporous silica nanoparticles for the controlled delivery of poorly water-soluble non-steroidal anti-inflammatory drugs, Acta Biomater. 134 (2021) 576–592, https://doi.org/10.1016/j.actbio.2021.07.023.

[3] I. Menon, M. Zaroudi, Y. Zhang, E. Aisenbrey, L. Hui, Fabrication of active targeting lipid nanoparticles: challenges and perspectives, Mater. Today Adv. 16 (2022) 100299, https://doi.org/10.1016/j.mtadv.2022.100299.

[4] C. Jiménez-Jiménez, A. Moreno-Borrallo, B. Dumontel, M. Manzano, M. Vallet-Regí, Biomimetic camouflaged nanoparticles with selective cellular internalization and migration competences, Acta Biomater. 157 (2023) 395–407, https://doi.org/10.1016/j.actbio.2022.11.059.

[5] S. Liu, D. Jiang, S. Qian, Z. Ren, J. Sun, J. Ye, W. Zhao, Hypoxia-adaptive penetration enhanced nanomedicine regulating cell–internalization ability enabling the uniform distribution within tumors, Chem. Eng. J. 505 (2025) 159136, https://doi.org/10.1016/j.cej.2024.159136.

[6] J.M. Steinbach, Y.-E. Seo, W.M. Saltzman, Cell penetrating peptide-modified poly (lactic-co-glycolic acid) nanoparticles with enhanced cell internalization, Acta Biomater. 30 (2016) 49–61, https://doi.org/10.1016/j.actbio.2015.11.029.

[7] K.-C. Lin, C.-Z. Yen, J.-W. Yang, J. Chung, G.-Y. Chen, Airborne toxicological assessment: the potential of lung-on-a-chip as an alternative to animal testing, Mater. Today Adv. 14 (2022) 100216, https://doi.org/10.1016/j.mtadv.2022.100216.

[8] J. Yan, X. Meng, Y. Zhu, Y. Jiang, Y. Wang, B. Zhang, Y. Xu, X. Ma, X. Sun, H. Liu, Remodeling the blood-air barrier and enhancing the pulmonary microcirculation with a dual-responsive biomimetic nanosystem for precise therapy in acute lung injury, Acta Biomater. 202 (2025) 573–590, https://doi.org/10.1016/j.actbio.2025.06.050.

[9] P. Pang, W. Liu, S. Ma, J. Liu, S. Wu, W. Xue, J. Zhang, X. Ji, Self-assembling natural flavonoid nanomedicines for alveolar macrophage reprogramming by restoring mitochondrial function in acute lung injury therapy, Chem. Eng. J. 506 (2025) 160171, https://doi.org/10.1016/j.cej.2025.160171.

[10] M. Ali, Pulmonary drug delivery, in: Handbook of Non-invasive Drug Delivery Systems, Elsevier, 2010, pp. 209–246, https://doi.org/10.1016/B978-0-8155-2025-2.10009-5.

[11] T. Duong, M. Vivero-Lopez, I. Ardao, C. Alvarez-Lorenzo, A. Forgács, J. Kalmár, C. A. García-González, Alginate aerogels by spray gelation for enhanced pulmonary delivery and solubilization of beclomethasone dipropionate, Chem. Eng. J. 485 (2024) 149849, https://doi.org/10.1016/j.cej.2024.149849.

[12] M. Pieterjan, V.H.L. De Backer Lynn, G. Roberta, E. Mercedes, B. Pieter, O. Bárbara, S. Xavier, P.-G. Jésus, C. De Smedt Stefaan, R. Koen, Surfactant protein B (SP-B) enhances the cellular siRNA delivery of proteolipid coated nanogels for inhalation therapy, Acta Biomater. 78 (2018) 236–246, https://doi.org/10.1016/j.actbio.2018.08.012.

[13] D. Groneberg, C. Witt, U. Wagner, K. Chung, A. Fischer, Fundamentals of pulmonary drug delivery, Respir. Med. 97 (4) (2003) 382–387, https://doi.org/10.1053/rmed.2002.1457.

[14] B. Wang, L. Wang, Q. Yang, Y. Zhang, T. Qinglai, X. Yang, Z. Xiao, L. Lei, S. Li, Pulmonary inhalation for disease treatment: basic research and clinical translations, Mater. Today Bio 25 (2024) 100966, https://doi.org/10.1016/j.mtbio.2024.100966.

[15] D.I. Daniher, J. Zhu, Dry powder platform for pulmonary drug delivery, Particuology 6 (4) (2008) 225–238, https://doi.org/10.1016/j.partic.2008.04.004.

[16] P. Muralidharan, M. Malapit, E. Mallory, D. Hayes Jr., H.M. Mansour, Inhalable nanoparticulate powders for respiratory delivery, Nanomed. Nanotechnol. Biol. Med. 11 (5) (2015) 1189–1199, https://doi.org/10.1016/j.nano.2015.01.007.

[17] L.-M. Xu, T.-T. Hu, Y. Pu, Y. Le, J.-F. Chen, J.-X. Wang, Preparation of high-performance ultrafine budesonide particles for pulmonary drug delivery, Chem. Eng. J. 252 (2014) 281–287, https://doi.org/10.1016/j.cej.2014.05.002.

[18] M. Miragoli, P. Ceriotti, M. Iafisco, M. Vacchiano, N. Salvarani, A. Alogna, P. Carullo, G.B. Ramirez-Rodríguez, T. Patrício, L.D. Esposti, Inhalation of peptide-loaded nanoparticles improves heart failure, Sci. Transl. Med. 10 (424) (2018) eaan6205, https://doi.org/10.1126/scitranslmed.aan6205.

[19] F. Gagnadoux, J. Hureaux, L. Vecellio, T. Urban, A. Le Pape, I. Valo, J. Montharu, V. Leblond, M. Boisdron-Celle, S. Lerondel, Aerosolized chemotherapy, J. Aerosol Med. Pulm. Drug Deliv. 21 (1) (2008) 61–70, https://doi.org/10.1089/jamp.2007.0656.

[20] O.B. Garbuzenko, G. Mainelis, O. Taratula, T. Minko, Inhalation treatment of lung cancer: the influence of composition, size and shape of nanocarriers on their lung accumulation and retention, Cancer Biol. Med. 11 (1) (2014) 44, https://doi.org/10.7497/j.issn.2095-3941.2014.01.004.

[21] S. Newman, M. Johnson, S. Clarke, Effect of particle size of bronchodilator aerosols on lung distribution and pulmonary function in patients with chronic asthma, Thorax 43 (2) (1988) 159, https://doi.org/10.1136/thx.43.2.159.

[22] P. Zanen, L. Go, J. Lammers, Optimal particle size for beta 2 agonist and anticholinergic aerosols in patients with severe airflow obstruction, Thorax 51 (10) (1996) 977–980, https://doi.org/10.1136/thx.51.10.977.

[23] P.J. Thompson, Drug delivery to the small airways, Am. J. Respir. Crit. Care Med. 157 (5) (1998) S199–S202, https://doi.org/10.1164/ajrccm.157.5.rsaa-7.

[24] C. Darquenne, Deposition mechanisms, J. Aerosol Med. Pulm. Drug Deliv. 33 (4) (2020) 181–185, https://doi.org/10.1089/jamp.2020.29029.cd.

[25] J. Blake, On the movement of mucus in the lung, J. Biomech. 8 (3–4) (1975) 179–190, https://doi.org/10.1016/0021-9290(75)90023-8.

[26] Q. Liu, J. Guan, L. Qin, X. Zhang, S. Mao, Physicochemical properties affecting the fate of nanoparticles in pulmonary drug delivery, Drug Discov. Today 25 (1) (2020) 150–159, https://doi.org/10.1016/j.drudis.2019.09.023.

[27] P. Chen, Z. Zhang, N. Gu, M. Ji, Effect of the surface charge density of nanoparticles on their translocation across pulmonary surfactant monolayer: a molecular dynamics simulation, Mol. Simul. 44 (2) (2018) 85–93, https://doi.org/10.1080/08927022.2017.1342118.

[28] R. Bessler, S. Bhardwaj, D. Malka, R. Fishler, J. Sznitman, Exploring the role of electrostatic deposition on inhaled aerosols in alveolated microchannels, Sci. Rep. 13 (1) (2023) 23069, https://doi.org/10.1038/s41598-023-49946-w.

[29] R. Bessler, J. Sznitman, The potential of leveraging electrostatics for improved inhaled drug delivery to the lungs, Front. Med. Eng. 1 (2024) 1298251, https://doi.org/10.3389/fmede.2023.1298251.

[30] M. Cazzola, F. Cavalli, O.S. Usmani, P. Rogliani, Advances in pulmonary drug delivery devices for the treatment of chronic obstructive pulmonary disease, Expet Opin. Drug Deliv. 17 (5) (2020) 635–646, https://doi.org/10.1080/17425247.2020.1739021.

[31] A.H. Chow, H.H. Tong, P. Chattopadhyay, B.Y. Shekunov, Particle engineering for pulmonary drug delivery, Pharm. Res. 24 (2007) 411–437, https://doi.org/10.1007/s11095-006-9174-3.

[32] I.M. El-Sherbiny, N.M. El-Baz, M.H. Yacoub, Inhaled nano-and microparticles for drug delivery, Glob. Cardiol. Sci. Pract. 2015 (1) (2015) 2, https://doi.org/10.5339/gcsp.2015.2.

[33] L. Louis, B. Simonassi-Paiva, M. McAfee, M.J. Nugent, Co-axial electrosprayed RAD001-loaded polycaprolactone/polyvinyl alcohol core–shell particles for treating pediatric brain tumours, Eur. J. Pharm. Biopharm. 201 (2024) 114376, https://doi.org/10.1016/j.ejpb.2024.114376.

[34] Z. Cai, H. Jiang, T. Lin, C. Wang, J. Ma, R. Gao, Y. Jiang, X. Zhou, Microspheres in bone regeneration: fabrication, properties and applications, Mater. Today Adv. 16 (2022) 100315, https://doi.org/10.1016/j.mtadv.2022.100315.

[35] Y. Wu, L. Li, Y. Mao, L.J. Lee, Static micromixer–coaxial electrospray synthesis of theranostic lipoplexes, ACS Nano 6 (3) (2012) 2245–2252, https://doi.org/10.1021/nn204300s.

[36] C. Zhang, Z.-C. Yao, Q. Ding, J.J. Choi, Z. Ahmad, M.-W. Chang, J.-S. Li, Tri-needle coaxial electrospray engineering of magnetic polymer yolk–shell particles possessing dual-imaging modality, multiagent compartments, and trigger release potential, ACS Appl. Mater. Interfaces 9 (25) (2017) 21485–21495, https://doi.org/10.1021/acsami.7b05580.

[37] X. Zhang, Q. Qu, A. Zhou, Y. Wang, J. Zhang, R. Xiong, V. Lenders, B. B. Manshian, D. Hua, S.J. Soenen, Core-shell microparticles: from rational engineering to diverse applications, Adv. Colloid Interface Sci. 299 (2022) 102568, https://doi.org/10.1016/j.cis.2021.102568.

[38] Z.-C. Yao, C. Zhang, Z. Xing, Z. Ahmad, Q. Ding, M.-W. Chang, Controlled engineering of multifunctional porous structures using tri-needle co-axial electrohydrodynamic flow and sacrificial media, Chem. Eng. J. 429 (2022) 132221, https://doi.org/10.1016/j.cej.2021.132221.

[39] J. Hou, Y. Yang, D.-G. Yu, Z. Chen, K. Wang, Y. Liu, G.R. Williams, Multifunctional fabrics finished using electrosprayed hybrid janus particles containing nanocatalysts, Chem. Eng. J. 411 (2021) 128474, https://doi.org/10.1016/j.cej.2021.128474.

[40] K. Zhao, Z. Hu, X. Rao, Y. Chen, M. Zhou, X. Li, F. Zhou, Z. Ding, M. Li, B. Zhu, An EHDA janus hybrids loaded with Bletilla striata polysaccharide and berberine for the treatment of diabetic ulcer, Eur. Polym. J. 212 (2024) 113085, https://doi.org/10.1016/j.eurpolymj.2024.113085.

[41] K. Yu, J. Chen, Q. Zhu, B. Li, X. Zuo, H. Lu, H. Zhang, J. Wang, Z. Wang, J. Pan, Easily recycled porous microparticles prepared via electrohydrodynamic atomization for selective uranium extraction with high capacity, ACS Sustain. Chem. Eng. 10 (44) (2022) 14600–14613, https://doi.org/10.1021/acssuschemeng.2c04621.

[42] T. He, J.V. Jokerst, Structured micro/nano materials synthesized via electrospray: a review, Biomater. Sci. 8 (20) (2020) 5555–5573, https://doi.org/10.1039/D0BM01313G.

[43] Q. Zhang, J. Liu, X. Wang, M. Li, J. Yang, Controlling internal nanostructures of porous microspheres prepared via electrospraying, Colloid Polym. Sci. 288 (2010) 1385–1391, https://doi.org/10.1007/s00396-010-2273-z.

[44] J. Gao, W. Li, J.S.-P. Wong, M. Hu, R.K. Li, Controllable morphology and wettability of polymer microspheres prepared by nonsolvent assisted electrospraying, Polymer 55 (12) (2014) 2913–2920, https://doi.org/10.1016/j.polymer.2014.04.033.

[45] H. Chen, J. Su, C.S. Brennan, P. Van der Meeren, N. Zhang, Y. Tong, P. Wang, Recent developments of electrospun zein nanofibres: strategies, fabrication and therapeutic applications, Mater. Today Adv. 16 (2022) 100307, https://doi.org/10.1016/j.mtadv.2022.100307.

[46] Y.A. Alli, A. Bamisaye, A.T. Onawole, P.O. Oladoye, O.M. Bankole, B. Koivisto, K. Youssef, Coaxial electrospinning: design, characterization, mechanistic insights and their emerging applications in solar cells, Nano Energy 131 (2024) 110203, https://doi.org/10.1016/j.nanoen.2024.110203.

[47] T.D. Khanh, J.S. Meena, S.B. Choi, J.-W. Kim, Breathable, self-healable, washable and durable all-fibrous triboelectric nanogenerator for wearable electronics, Mater. Today Adv. 20 (2023) 100427, https://doi.org/10.1016/j.mtadv.2023.100427.

[48] N.L. Mai, T.V.A. Hoang, T.-H. Vu, H.-D. Vu, C. Doan, Y. Yong, T.X. Dinh, D. Dao, V.T. Dau, Pulsated in-Situ dried electrostretching fabrication of microneedles for transdermal drug delivery. 2025 23rd International Conference on Solid-State Sensors, Actuators and Microsystems (Transducers), IEEE, 2025, pp. 550–553, https://doi.org/10.1109/Transducers61432.2025.11110014.

[49] N.L. Mai, Y. Yong, T.V.A. Hoang, T.H. Vu, H.D. Vu, V.C. Doan, D. Cai, T.X. Dinh, D.V. Dao, V.T. Dau, Fabrication of microneedles by pulsating in situ dried electrostretching for transdermal drug delivery, Small Methods (2025) 2500183, https://doi.org/10.1002/smtd.202500183.

[50] H.-D. Vu, T.-H. Vu, N.L. Mai, D.C. Pande, D.V. Dao, B.H. Rehm, N.-T. Nguyen, G. D. Grant, C.-D. Tran, Y. Zhu, In-flight electro-neutralisation electrospray for pulmonary drug delivery, Nano Today 55 (2024) 102217, https://doi.org/10.1016/j.nantod.2024.102217.

[51] J.C. Ijsebaert, K.B. Geerse, J.C. Marijnissen, J.-W.J. Lammers, P. Zanen, Electro-hydrodynamic atomization of drug solutions for inhalation purposes, J. Appl. Physiol. 91 (6) (2001) 2735–2741, https://doi.org/10.1152/jappl.2001.91.6.2735.

[52] L. Golshahi, P.W. Longest, L. Holbrook, J. Snead, M. Hindle, Production of highly charged pharmaceutical aerosols using a new aerosol induction charger, Pharm. Res. 32 (2015) 3007–3017, https://doi.org/10.1007/s11095-015-1682-6.

[53] T.-H. Vu, S. Yadav, C.-D. Tran, H.-Q. Nguyen, T.-H. Nguyen, T. Nguyen, T.-K. Nguyen, J.W. Fastier-Wooller, T. Dinh, H.-P. Phan, Charge-reduced particles via self-propelled electrohydrodynamic atomization for drug delivery applications, ACS Appl. Mater. Interfaces 15 (25) (2023) 29777–29788, https://doi.org/10.1021/acsami.3c02000.

[54] T. Ciach, Application of electro-hydro-dynamic atomization in drug delivery, J. Drug Deliv. Sci. Technol. 17 (6) (2007) 367–375, https://doi.org/10.1016/S1773-2247(07)50076-6.

[55] J. Borra, D. Camelot, K.-L. Chou, P. Kooyman, J. Marijnissen, B. Scarlett, Bipolar coagulation for powder production: micro-mixing inside droplets, J. Aerosol Sci. 30 (7) (1999) 945–958, https://doi.org/10.1016/S0021-8502(98)00757-5.

[56] J. Borra, D. Camelot, J. Marijnissen, B. Scarlett, A new production process of powders with defined properties by electrohydrodynamic atomization of liquids and post-production electrical mixing, J. Electrost. 40 (1997) 633–638, https://doi.org/10.1016/S0304-3886(97)00065-X.

[57] S. Park, U. Cvelbar, W. Choe, S.Y. Moon, The creation of electric wind due to the electrohydrodynamic force, Nat. Commun. 9 (1) (2018) 371, https://doi.org/10.1038/s41467-017-02766-9.

[58] L.Y. Yeo, D. Lastochkin, S.-C. Wang, H.-C. Chang, A new ac electrospray mechanism by maxwell-wagner polarization and capillary resonance, Phys. Rev. Lett. 92 (13) (2004) 133902, https://doi.org/10.1103/PhysRevLett.92.133902.

[59] P. Wang, S. Maheshwari, H.-C. Chang, Polyhedra formation and transient cone ejection of a resonant microdrop forced by an ac electric field, Phys. Rev. Lett. 96 (25) (2006) 254502, https://doi.org/10.1103/PhysRevLett.96.254502.

[60] D.B. Bober, C.-H. Chen, Pulsating electrohydrodynamic cone-jets: from choked jet to oscillating cone, J. Fluid Mech. 689 (2011) 552–563, https://doi.org/10.1017/jfm.2011.453.

[61] V.T. Dau, T.-K. Nguyen, D.V. Dao, Charge reduced nanoparticles by sub-kHz ac electrohydrodynamic atomization toward drug delivery applications, Appl. Phys. Lett. 116 (2) (2020), https://doi.org/10.1063/1.5133714.

[62] E. Demekhin, S. Polyanskikh, A. Ramos, Taylor cones in a leaky dielectric liquid under an ac electric field, physical review E—statistical, nonlinear, and, Soft Matter Phy. 84 (3) (2011) 035301, https://doi.org/10.1103/PhysRevE.84.035301.

[63] N. Chetwani, C.A. Cassou, D.B. Go, H.-C. Chang, Frequency dependence of alternating current electrospray ionization mass spectrometry, Anal. Chem. 83 (8) (2011) 3017–3023, https://doi.org/10.1021/ac103189p.

[64] Y. Ju, C. Cortez-Jugo, J. Chen, T.Y. Wang, A.J. Mitchell, E. Tsantikos, N. Bertleff-Zieschang, Y.W. Lin, J. Song, Y. Cheng, Engineering of nebulized metal–phenolic capsules for controlled pulmonary deposition, Adv. Sci. 7 (6) (2020) 1902650, https://doi.org/10.1002/advs.201902650.

[65] Y. Zhou, T.L. Brasel, D. Kracko, Y.-S. Cheng, A. Ahuja, J.P. Norenberg, H. William Kelly, Influence of impactor operating flow rate on particle size distribution of four jet nebulizers, Pharmaceut. Dev. Technol. 12 (4) (2007) 353–359, https://doi.org/10.1080/10837450701366937.

[66] I.O.f. Standardization, ISO 27427:2013: Anaesthetic and Respiratory Equipment - Nebulizing Systems and Components, International Organization for Standardization, 2013.

[67] J.P. Mitchell, M.W. Nagel, Cascade impactors for the size characterization of aerosols from medical inhalers: their uses and limitations, J. Aerosol Med. 16 (4) (2003) 341–377, https://doi.org/10.1089/089426803772455622.

[68] T.X. Dinh, T.T. Bui, T. Terebessy, Bipolar Corona assisted jet flow for fluidic application, Flow Meas. Instrum. 50 (2016) 252–260, https://doi.org/10.1016/j.flowmeasinst.2016.07.005.

[69] T.X. Dinh, C.-D. Tran, T. Terebessy, T.C. Duc, T.T. Bui, Particle precipitation by bipolar Corona discharge ion winds, J. Aerosol Sci. 124 (2018) 83–94, https://doi.org/10.1016/j.jaerosci.2018.07.007.

[70] W. Xu, R. Jiang, M. Xu, M.S. Hasan, K. Polifrone, J. Gu, Y. Yang, E. Torresani, E. Olevsky, Localized engineering of grain boundary morphology by electro-nano-pulsing processing, Mater. Today Adv. 20 (2023) 100442, https://doi.org/10.1016/j.mtadv.2023.100442.

[71] S.J. Gaskell, Electrospray: principles and practice, J. Mass Spectrom. 32 (7) (1997) 677–688, https://doi.org/10.1002/(SICI)1096-9888(199707)32:7%3C677::AID-JMS536%3E3.0.CO;2-G.

[72] J. Melcher, G. Taylor, Electrohydrodynamics: a review of the role of interfacial shear stresses, Annu. Rev. Fluid Mech. 1 (1) (1969) 111–146, https://doi.org/10.1146/annurev.fl.01.010169.000551.

[73] L.N. Mai, T.H. Vu, T.X. Dinh, H.D. Vu, C.-D. Tran, V.T. Dau, H.K. Ngo, Numerical study of electrohydrodynamic atomization considering liquid wetting and Corona discharge effects, Phys. Fluids 35 (6) (2023), https://doi.org/10.1063/5.0151085.

[74] N.L. Mai, T.H. Vu, H.-D. Vu, C. Doan, Y. Yong, T.X. Dinh, D.V. Dao, V.T. Dau, Evaporation in electrohydrodynamic atomisation: a numerical and experimental investigation, Int. Commun. Heat Mass Tran. 165 (2025) 109079, https://doi.org/10.1016/j.icheatmasstransfer.2025.109079.

[75] H. Kim, Y. Teramoto, A. Negishi, A. Ogata, J. Kim, B. Pongrác, Z. Machala, A. M. Gañán-Calvo, Polarity effect on the electrohydrodynamic (EHD) spray of

water, J. Aerosol Sci. 76 (2014) 98–114, https://doi.org/10.1016/j.jaerosci.2014.06.002.

[76] B. Tarabová, P. Lukeš, M. Janda, K. Hensel, L. Šikurová, Z. Machala, Specificity of detection methods of nitrites and ozone in aqueous solutions activated by air plasma, Plasma Process. Polym. 15 (6) (2018) 1800030, https://doi.org/10.1002/ppap.201800030.

[77] A. Smeets, C. Clasen, G. Van den Mooter, Electrospraying of polymer solutions: study of formulation and process parameters, Eur. J. Pharm. Biopharm. 119 (2017) 114–124, https://doi.org/10.1016/j.ejpb.2017.06.010.

[78] J. Xie, J. Jiang, P. Davoodi, M.P. Srinivasan, C.-H. Wang, Electrohydrodynamic atomization: a two-decade effort to produce and process micro-/nanoparticulate materials, Chem. Eng. Sci. 125 (2015) 32–57, https://doi.org/10.1016/j.ces.2014.08.061.

[79] F.A.A. Lajhar, Electrospray for Pulmonary Drug Delivery, The University of Manchester, United Kingdom, 2018.

[80] T.-H. Vu, H.T. Nguyen, J.W. Fastier-Wooller, C.-D. Tran, T.-H. Nguyen, H.-Q. Nguyen, T. Nguyen, T.-K. Nguyen, T. Dinh, T.T. Bui, Enhanced electrohydrodynamics for electrospinning a highly sensitive flexible fiber-based piezoelectric sensor, ACS Appl. Electron. Mater. 4 (3) (2022) 1301–1310, https://doi.org/10.1021/acsaelm.2c00030.

[81] J.Y. Kim, S.J. Lee, J.G. Hong, Spray mode and monodisperse droplet properties of an electrospray, ACS Omega 7 (32) (2022) 28667–28674, https://doi.org/10.1021/acsomega.2c04002.

[82] A. Gomez, The electrospray: fundamentals and applications, experimental heat transfer, J. Fluid Mech. 1993 (1993) 270–282, https://doi.org/10.1016/B978-0-444-81619-1.50028-9.

[83] H. Lee, S. An, K. Bin, B. Jeon, M. Kim, I.S. Kim, Readily functionalizable and stabilizable polymeric particles with controlled size and morphology by electrospray, Sci. Rep. 8 (1) (2018) 15725.

[84] J. Xie, J.C. Marijnissen, C.-H. Wang, Microparticles developed by electrohydrodynamic atomization for the local delivery of anticancer drug to treat C6 glioma in vitro, Biomaterials 27 (17) (2006) 3321–3332, https://doi.org/10.1016/j.biomaterials.2006.01.034.

[85] A.C. Anderson, M.N. Dubosky, K.A. Fiorino, V. Quintana, C.A. Kaplan, D.L. Vines, The effect of nebulizer position on aerosolized epoprostenol delivery in an adult lung model, Respir. Care 62 (11) (2017) 1387–1395.

[86] K. McDermott, J.G. Oakley, Droplet size and distribution of nebulized 3% sodium chloride, albuterol, and epoprostenol by phase doppler particle analyzer, Curr. Ther. Res. 94 (2021) 100623, https://doi.org/10.1016/j.curtheres.2021.100623.

[87] M. McPeck, G.C. Smaldone, Continuous infusion aerosol delivery of prostacyclins during mechanical ventilation: challenges, limitations, and recent advances, Expet Opin. Drug Deliv. 19 (5) (2022) 465–474, https://doi.org/10.1080/17425247.2022.2061460.

[88] R. Xue, X. Geng, F. Liang, Y. Liu, W. Yang, Z. Huang, Natural plant compounds in synthesis and luminescence modulation of metal nanoclusters: toward sustainable nanoprobes for sensing and bioimaging, Mater. Today Adv. 16 (2022) 100279, https://doi.org/10.1016/j.mtadv.2022.100279.

[89] H. Xu, T. Wang, C. Yang, X. Li, G. Liu, Z. Yang, P.K. Singh, S. Krishnan, D. Ding, Supramolecular nanofibers of curcumin for highly amplified radiosensitization of colorectal cancers to ionizing radiation, Adv. Funct. Mater. 28 (14) (2018) 1707140, https://doi.org/10.1002/adfm.201707140.

[90] R. Blomberg, K. Sompel, C. Hauer, A.J. Smith, B. Peña, J. Driscoll, P.S. Hume, D.T. Merrick, M.A. Tennis, C.M. Magin, Hydrogel-embedded precision-cut lung slices model lung cancer premalignancy Ex vivo, Adv. Healthcare Mater. 13 (4) (2024) 2302246, https://doi.org/10.1002/adhm.202302246.

[91] Y. Jia, Y. Zhang, W. Zhan, Y. Wang, X. Sun, Y. Zhang, X. Liu, B. Han, Y. Bai, L. Shen, Sustained release of neuroprotective drugs curcumin and edaravone from supramolecular hydrogel for ischemic stroke treatment, Adv. Funct. Mater. 33 (49) (2023) 2303930, https://doi.org/10.1002/adfm.202303930.

[92] L. Yue, C. Gao, J. Li, H. Chen, S.M. Lee, R. Luo, R. Wang, Chemotaxis-guided self-propelled macrophage motor for targeted treatment of acute pneumonia, Adv. Mater. 35 (20) (2023) 2211626, https://doi.org/10.1002/adma.202211626.

[93] M. Kharat, Z. Du, G. Zhang, D.J. McClements, Physical and chemical stability of curcumin in aqueous solutions and emulsions: impact of pH, temperature, and molecular environment, J. Agric. Food Chem. 65 (8) (2017) 1525–1532, https://doi.org/10.1021/acs.jafc.6b04815.

[94] P.P. Dandekar, V.B. Patravale, Development and validation of a stability-indicating LC method for curcumin, Chromatographia 69 (9) (2009) 871–877, https://doi.org/10.1365/s10337-009-0995-1.

[95] Z. Mai, J. Chen, T. He, Y. Hu, X. Dong, H. Zhang, W. Huang, F. Ko, W. Zhou, Electrospray biodegradable microcapsules loaded with curcumin for drug delivery systems with high bioactivity, RSC Adv. 7 (3) (2017) 1724–1734, https://doi.org/10.1039/C6RA25314H.

[96] S. Chen, D.J. McClements, L. Jian, Y. Han, L. Dai, L. Mao, Y. Gao, Core–shell biopolymer nanoparticles for co-delivery of curcumin and piperine: sequential electrostatic deposition of hyaluronic acid and chitosan shells on the zein core, ACS Appl. Mater. Interfaces 11 (41) (2019) 38103–38115, https://doi.org/10.1021/acsami.9b11782.

[97] N.H.T. Luu, H.Q. Ly, C.V. Nguyen, L.T.T. Dinh, T.K.N. Nguyen, C.M. Phan, M.L. Nguyen, H.H. Vu, C.H. Luu, T.T. Hoang Thi, Cholesterol-conjugated PAMAM dendrimers: enhancing stability, drug delivery efficiency, and in vitro anticancer performance, J. Polym. Sci. 63 (3) (2024) 541–553, https://doi.org/10.1002/pol.20240933.

[98] F. Wang, G.M. Saidel, J. Gao, A mechanistic model of controlled drug release from polymer millirods: effects of excipients and complex binding, J. Contr. Release 119 (1) (2007) 111–120, https://doi.org/10.1016/j.jconrel.2007.01.019.

[99] V.S. Saji, Supramolecular organic nanotubes for drug delivery, Mater. Today Adv. 14 (2022) 100239, https://doi.org/10.1016/j.mtadv.2022.100239.

[100] C.M. Phan, C.H. Luu, M. Murugesan, N.-Y.N. Ha, H.L. Ngo, N.-D.H. Nguyen, Z. Pan, V.G. Phan, Y. Li, T. Thambi, Injectable gelatin-pectin hydrogel for dental tissue engineering: enhanced angiogenesis and antibacterial efficacy for pulpitis therapy, Int. J. Biol. Macromol. 284 (2024) 137939, https://doi.org/10.1016/j.ijbiomac.2024.137939.

[101] C.H. Luu, D.T.D. Nguyen, C.Y. Chee, T.C.N. Thi, D.Y.P. Nguyen, D.H. Nguyen, C.K. Nguyen, Thermal and redox responsive polyamidoamine dendrimer–poly (N-isopropylacrylamide) bridged by disulfide linkages for targeted and controlled drug delivery system, J. Appl. Polym. Sci. 140 (27) (2023) e54108, https://doi.org/10.1002/app.54108.

[102] G. Wang, Z. Zhai, W. Wang, X. Xia, H. Guo, X. Yue, X. Wang, B. Zhu, Z. Huang, X. Pan, Tailored borneol-modified lipid nanoparticles nasal spray for enhanced nose-to-brain delivery to central nervous system diseases, ACS Nano 18 (34) (2024) 23684–23701, https://doi.org/10.1021/acsnano.4c08279.

[103] V. Neiens, E.-M. Hansbauer, T.J. Jaquin, J.K. Peper-Gabriel, P. Mahavadi, M.E. Snyder, M.J. Grill, C. Wurzenberger, A. Konitsiotis, A. Estrada-Bernal, Preclinical concept studies showing advantage of an inhaled anti-CTGF/CCN2 protein for pulmonary fibrosis treatment, Nat. Commun. 16 (1) (2025) 3251, https://doi.org/10.1038/s41467-025-58568-x.

[104] B.E. Buchan, Formulation studies on cysteamine for the treatment of nephropathic cystinosis. http://hdl.handle.net/10059/701, 2011.

[105] K. May, The Cascade impactor, J. Sci. Instrum. 22 (10) (1945) 187, https://doi.org/10.1088/0950-7671/22/12/515.

[106] G. Newton, O. Raabe, B. Mokler, Cascade impactor design and performance, J. Aerosol Sci. 8 (5) (1977) 339–347, https://doi.org/10.1016/0021-8502(77)90021-0.

[107] P. Paul, S. Sengupta, B. Mukherjee, T.K. Shaw, R.H. Gaonkar, M.C. Debnath, Chitosan-coated nanoparticles enhanced lung pharmacokinetic profile of voriconazole upon pulmonary delivery in mice, Nanomedicine 13 (5) (2018) 501–520, https://doi.org/10.2217/nnm-2017-0291.

[108] C. Amador, C. Weber, M.A. Varacallo, Anatomy, Thorax, Bronchial, StatPearls, 2023. https://www.ncbi.nlm.nih.gov/sites/books/NBK537353/.

[109] M. Dunnill, G. Massarella, J. Anderson, A comparison of the quantitative anatomy of the bronchi in normal subjects, in status asthmaticus, in chronic bronchitis, and in emphysema, Thorax 24 (2) (1969) 176–179, https://doi.org/10.1136/thx.24.2.176.

[110] C. Guo, S.R. Gillespie, J. Kauffman, W.H. Doub, Comparison of delivery characteristics from a combination metered-dose inhaler using the andersen Cascade impactor and the next generation pharmaceutical impactor, J. Pharmaceut. Sci. 97 (8) (2008) 3321–3334, https://doi.org/10.1002/jps.21203.

[111] C. Majoral, A.L. Coates, A. Le Pape, L. Vecellio, Humidified and heated Cascade impactor for aerosol sizing, Front. Bioeng. Biotechnol. 8 (2020) 589782, https://doi.org/10.3389/fbioe.2020.589782.

[112] O. Mišík, J. Kejíková, O.e Cejpek, M. Malý, A. Jugl, M. Bělka, F. Mravec, F. Lizal, Nebulization and in vitro upper airway deposition of liposomal carrier systems, Mol. Pharm. 21 (4) (2024) 1848–1860, https://doi.org/10.1021/acs.molpharmaceut.3c01146.

[113] K.P. Fennelly, M.D. Tribby, C.-Y. Wu, G.L. Heil, L.J. Radonovich, J.C. Loeb, J.A. Lednicky, Collection and measurement of aerosols of viable influenza virus in liquid media in an andersen cascade impactor, Virus Adapt. Treat. 7 (2014) 1–9, https://doi.org/10.2147/VAAT.S74789.

[114] H. Okamoto, Y. Takeda, T. Okuda, An in vitro analysis of pulmonary deliverability of inhalable solutions and inhalable aerosol products dispersed in ventilator circuit, Aerosol. Sci. Technol. 59 (4) (2025) 388–401, https://doi.org/10.1080/02786826.2025.2449667.

[115] J.A. Kumar, S. Verma, S. Patel, N. Gupta, M. Patel, T. Kharidia, B. Gangadia, S. Butani, Engineering budesonide microparticles for enhancing pulmonary targeting: validation through in vivo investigations, Part. Part. Syst. Char. 42 (3) (2025) 2400139, https://doi.org/10.1002/ppsc.202400139.

[116] V. Espinosa, A. Rivera, First line of defense: innate cell-mediated control of pulmonary aspergillosis, Front. Microbiol. 7 (2016) 272, https://doi.org/10.3389/fmicb.2016.00272.

[117] M.T. Basel, S. Balivada, T.B. Shrestha, G.M. Seo, M.M. Pyle, M. Tamura, S.H. Bossmann, D.L. Troyer, A cell-delivered and cell-activated SN38-dextran prodrug increases survival in a murine disseminated pancreatic cancer model, Small 8 (6) (2012) 913–920, https://doi.org/10.1002/smll.201101879.

[118] P. Hai, T. Imai, S. Xu, R. Zhang, R.L. Aft, J. Zou, L.V. Wang, High-throughput, label-free, single-cell photoacoustic microscopy of intratumoral metabolic heterogeneity, Nat. Biomed. Eng. 3 (5) (2019) 381–391, https://doi.org/10.1038/s41551-019-0376-5.

[119] L.-L. Chen, C. Morcelle, Z.-L. Cheng, X. Chen, Y. Xu, Y. Gao, J. Song, Z. Li, M.D. Smith, M. Shi, Itaconate inhibits TET DNA dioxygenases to dampen inflammatory responses, Nat. Cell Biol. 24 (3) (2022) 353–363, https://doi.org/10.1038/s41556-022-00853-8.

[120] Y. Li, C. Guo, Q. Chen, Y. Su, H. Guo, R. Liu, C. Sun, S. Mi, J. Wang, D. Chen, Improvement of pneumonia by curcumin-loaded bionanosystems based on platycodon grandiflorum polysaccharides via calming cytokine storm, Int. J. Biol.

Macromol. 202 (2022) 691–706, https://doi.org/10.1016/j.ijbiomac.2022.01.194.

[121] S. Wu, P. Guo, Q. Zhou, X. Yang, J. Dai, Reprint of: M1 macrophage-targeted curcumin nanocrystals with l-arginine-modified for acute lung injury by inhalation, J. Pharmaceut. Sci. 114 (1) (2025) 105–118, https://doi.org/10.1016/j.xphs.2024.12.001.

[122] I.O.f. Standardization, ISO 10993-5:2009: Biological Evaluation of Medical Devices, ISO, Geneva, Switzerland, 2009.

Supplementary materials

Particle Self-Neutralization for Highly Efficient Deep Lung Delivery via Bipolar Electrohydrodynamic Atomization

Van Canh Doan [a*], Ngoc Luan Mai [a], Cuong Hung Luu [b], Donglin Cai [c], Wendong Gao [d], Trung Hieu Vu [a], Hoai Duc Vu [a], Thi Van Anh Hoang [a], Duc Khanh Tran [a], Dzung Dao [a], Hang Thu Ta [b], Yin Xiao [c], Peter Woodfield [a], Van Thanh Dau [a**]

Author affiliations

[a] School of Engineering and Built Environment, Griffith University, Queensland, AUSTRALIA

[b] School of Environment and Science, Griffith University, QLD, Australia

[c] School of Medicine and Dentistry, Griffith University, QLD, Australia

[d] Central Analytical Research Facility, Queensland University of Technology, Queensland, Australia

Corresponding author emails

[*]vancanh.doan@griffithuni.edu.au

[**]v.dau@griffith.edu.au

Section S1. Numerical simulation model of bipolar electrospray

Section S1.1. Governing equations

This work employs the Taylor-Melcher's leaky-dielectric model [1] providing a set of governing equations to account for the fluid dynamics and electrostatic conditions involved in electrospray. For fluid dynamics, we have the continuity and the momentum equations

$$\frac{\partial \rho}{\partial t} + \nabla \cdot (\rho \boldsymbol{u}) = 0, \tag{1}$$

$$\rho \left[\frac{\partial \boldsymbol{u}}{\partial t} + (\boldsymbol{u} \cdot \nabla) \boldsymbol{u} \right] = -\nabla p + \eta \nabla^2 \boldsymbol{u} + \boldsymbol{f}_\sigma + \boldsymbol{f}_e + \rho \boldsymbol{g}, \tag{2}$$

where ρ is the fluid density, t is the time, $\boldsymbol{u}$ is the fluid velocity, p is the pressure, η is the fluid viscosity, $\boldsymbol{g}$ is the gravitational acceleration, $\boldsymbol{f}_\sigma$, $\boldsymbol{f}_e$ are the surface tension force and electrostatic force, respectively. The physical properties of the air and isopropyl alcohol (IPA) are listed in the table S1. The surface tension force is calculated by the continuum surface force (CSF) model [2]

$$\boldsymbol{f}_\sigma = \sigma \kappa \nabla \gamma_{liq} = -\sigma \nabla \cdot \left(\frac{\nabla \gamma_{liq}}{|\nabla \gamma_{liq}|} \right) \nabla \gamma_{liq}, \tag{3}$$

with σ is the surface tension, κ is the mean curvature of the free surface, and the phase fraction of liquid γ_{liq} solved by the VOF method [3]

$$\frac{\partial \gamma_{liq}}{\partial t} + \nabla \cdot (\gamma_{liq}\boldsymbol{u}) + \nabla \cdot (\gamma_{liq}(1 - \gamma_{liq})\boldsymbol{u_r}) = 0, \tag{4}$$

where $\boldsymbol{u_r}$ is an artificial term for higher interface resolution [4].

Fluid density and viscosity are defined via

$$\begin{aligned} \rho &= \rho_1\gamma_{liq} + \rho_2(1 - \gamma_{liq}), \\ \mu &= \mu_1\gamma_{liq} + \mu_2(1 - \gamma_{liq}). \end{aligned} \tag{5}$$

For electrostatics, governing equations are solved iteratively to obtain the electrostatic force $\boldsymbol{f}_e$. Firstly, Gauss's law is involved

$$\nabla \cdot (\varepsilon\boldsymbol{E}) = \rho_e, \tag{6}$$

The Poisson's equation is derived by integrating Eq. 6 with the relation $\boldsymbol{E} = -\nabla\phi$

$$\nabla^2(\phi) = \frac{-\rho_e}{\varepsilon}, \tag{7}$$

in which ε is permittivity of the fluids, ϕ is the electric potential and ρ_e is the volumetric charge density. The conservation of charge equation is then considered

$$\frac{\partial \rho_e}{\partial t} + \nabla \cdot \boldsymbol{J} = 0, \tag{8}$$

with $\boldsymbol{J}$ is the current density, which is the ohmic charge conduction and the charge convection in the fluidic flow, so Eq. 8 can be rewritten as

$$\frac{\partial \rho_e}{\partial t} + \nabla \cdot (\rho_e\boldsymbol{u}) + \nabla \cdot (\kappa_e\boldsymbol{E}) = 0, \tag{9}$$

where κ_e is the electrical conductivity of the fluid. The electrical conductivity and permittivity are defined by harmonic averages [5]

$$\begin{aligned} \frac{1}{\varepsilon} &= \frac{\gamma_{liq}}{\varepsilon_1} + \frac{1 - \gamma_{liq}}{\varepsilon_2}, \\ \frac{1}{\kappa_e} &= \frac{\gamma_{liq}}{\kappa_{e1}} + \frac{1 - \gamma_{liq}}{\kappa_{e2}}. \end{aligned} \tag{10}$$

For incompressible fluids, electrostatic force is the Coulombic force and polarization force [6]

$$\boldsymbol{f}_e = \rho_e\boldsymbol{E} - \frac{1}{2}|\boldsymbol{E}|^2\nabla\varepsilon. \tag{11}$$
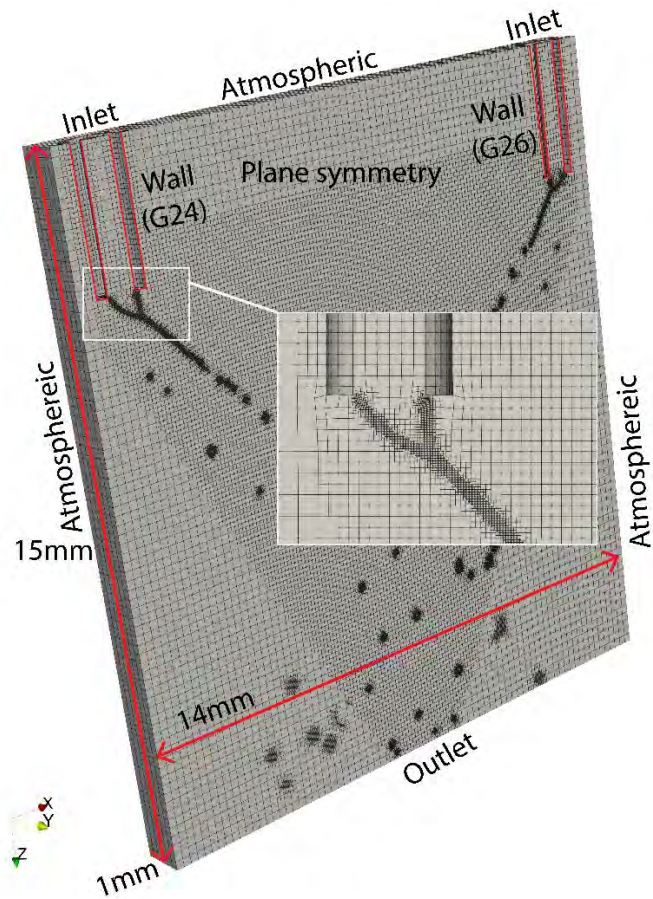
Section S1.2. Meshing and Boundary Conditions

The mesh in this work, shown in Fig. s2, was generated by snappyHexMesh, a built-in tool of OpenFOAM. Furthermore, adaptive mesh refinement was also utilized to avoid great computational cost. The base mesh size was 200µm and the mesh in the vicinity of the liquid/air interface was refined upto 4 levels (12.5µm). The boundary conditions of each face in the domain are listed in Table s2.
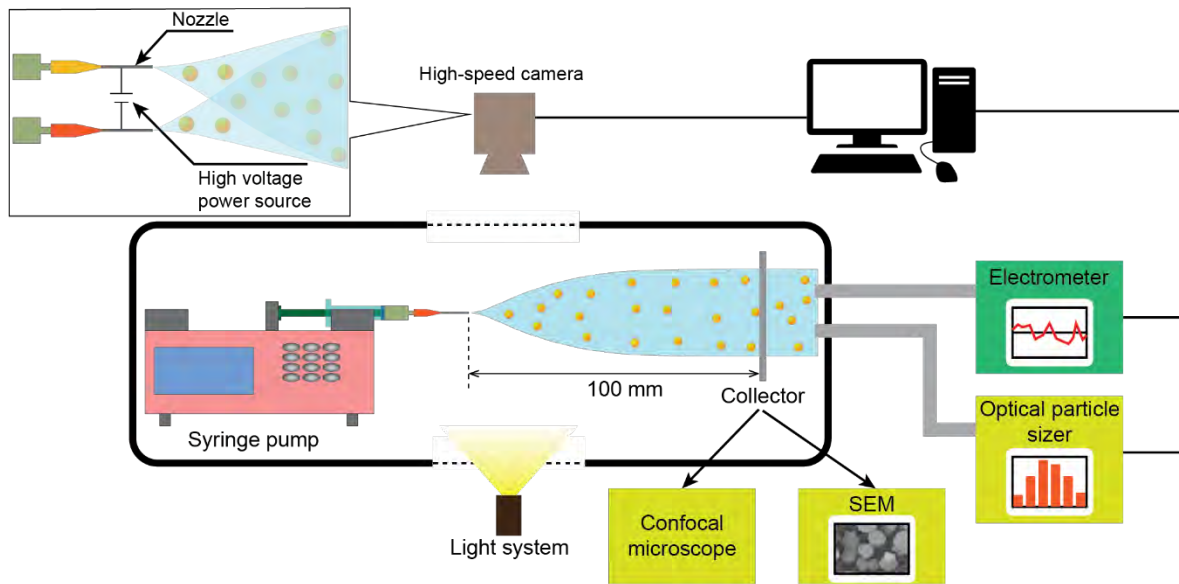
Figure S1: Experiment setup. 2 nozzles are different size 24G-26G (Muashi Engineering, Japan), Syring pump NE1000 (New Era Pump Systems Inc), 1 ml syringes (Terumo), High speed camera X9 PRO (Mega Speed), Collector is 45 um pore size membrane filter 47 mm diameter (Sigma Aldrich), Scanning electron microscope XL G2 (Phenom), Confocal microscope FV3000 (Olympus), Aerosol electrometer 3068B (TSI), Optical particle sizer 3330 (TSI).

Figure S2: Simulation domain, boundary conditions and meshing.
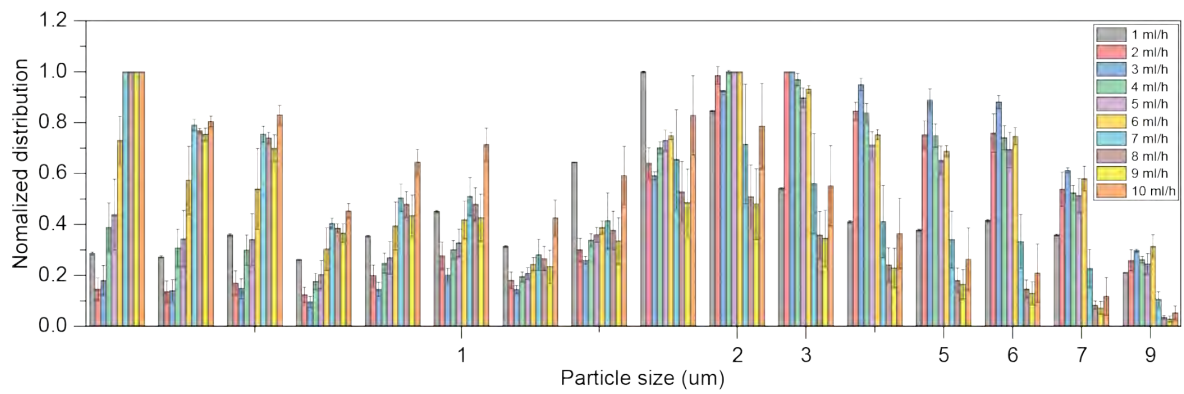
Figure s3: Particle size data at different flowrate with the nozzle pair 24G-26G. At low flow rates ranging from 1 to 5 ml/h, the particles were relatively uniform, with diameters primarily between 2 and 4 μm. However, when the flow rate was increased to 5 ml/h or higher, the particles became less uniform, with most having diameters below 0.5 μm.
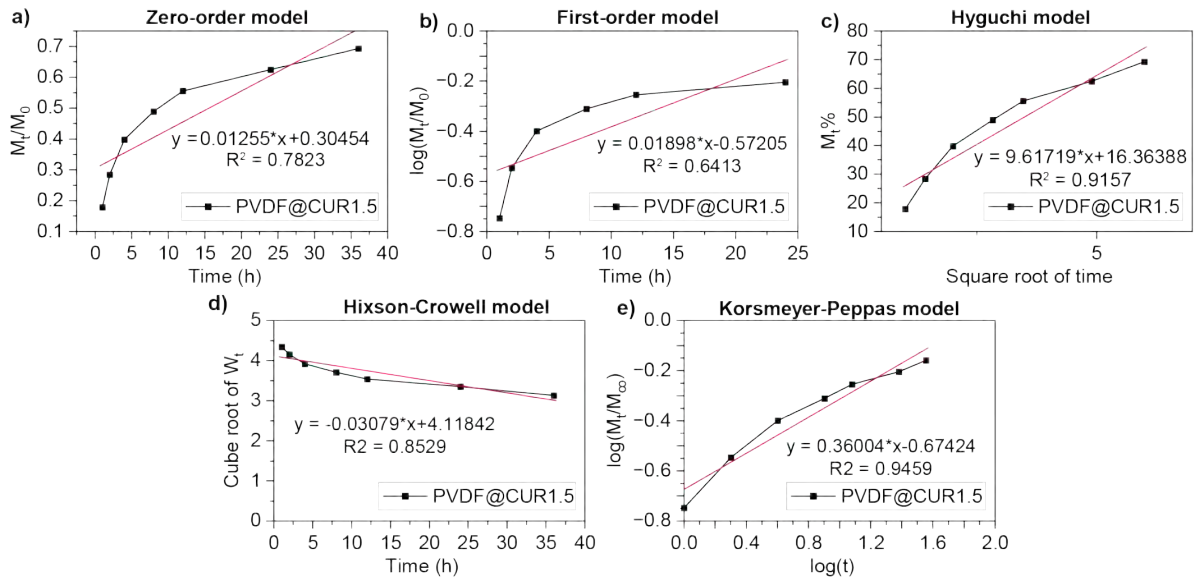
Figure s4: Release profile fitting of the concentration PVDF@CUR1.5, the red lines are fitting lines. The closest is Hyguchi model and Korsmeyer-Peppas model with R2 = 0.9157 and R2 = 0.9459, respectively. Those fittings suggest the drug release mechanism**.**
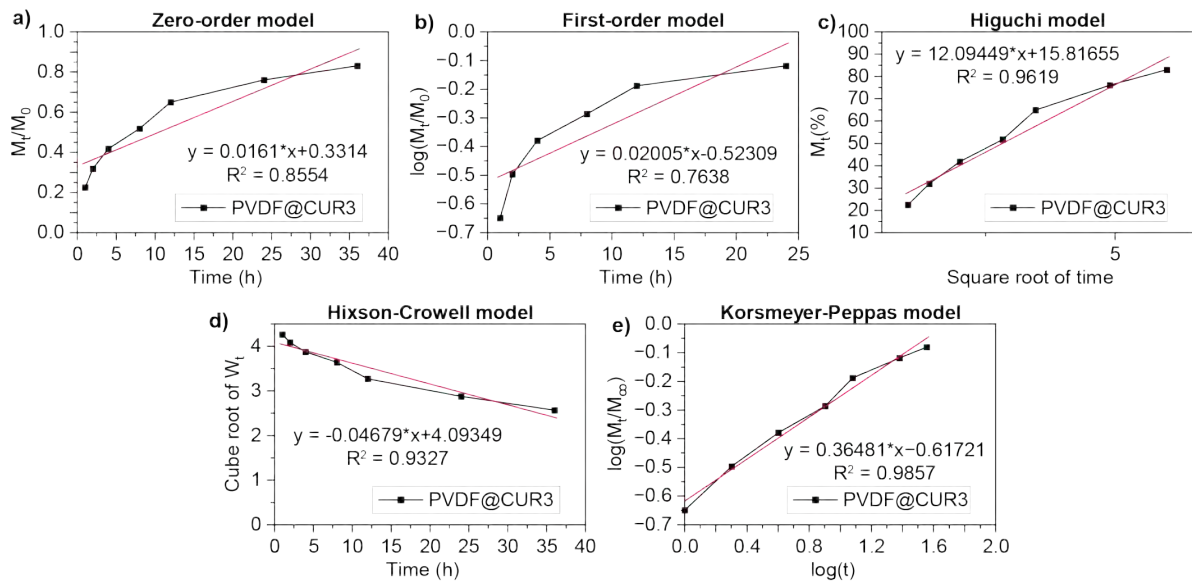
Figure s5: Release profile fitting of the concentration PVDF@CUR3, the red lines are fitting lines. Similar with CUR 1.5%, the closest is Hyguchi model and Korsmeyer-Peppas model with $R^2 = 0.9619$ and $R^2 = 0.9857$, respectively. Those fittings suggest the drug release mechanism.

List of Tables

Table S1: Physical properties of air and IPA

Fluid	Air	IPA
Density ρ (kg/m^3)	1.225	785
Dynamic Viscosity η (Pa. s)	1.813×10^{-5}	0.00166
Surface tension σ (N/m)	N/A	0.0208
Dielectric constant ε_r	1	18.6
Conductivity κ_e (mS/m)	1×10^{-9}	6×10^{-3}

Table S2: Boundary conditions for the simulation domain

Boundary	Fluidic conditions	Electrostatic conditions
Inlet	$u_x = 0; u_z = \dfrac{4Q}{\pi(i.d)^2}$ $\gamma_{liq} = 1$	$\nabla\phi = 0$
Nozzle 's wall (24G and 26G)	$u_x = u_z = 0$ (no slip);	$\phi = \phi_0$
Outlet	$p = p_0$	$\nabla\phi = 0$
Atmospheric	$p = p_0$	$\nabla\phi = 0$
Plane symmetry	$\dfrac{du_y}{dx} = 0$	$\dfrac{d\phi}{dx} = 0$

Table S3: Nozzle diameter information

Nozzle	Inner diameter (mm)	Outer diameter (mm)
15G	1.43	1.83
16G	1.26	1.65
17G	1.06	1.50
18G	0.97	1.27
19G	0.78	1.08
20G	0.66	0.90
21G	0.57	0.81
22G	0.47	0.72
23G	0.40	0.64
24G	0.31	0.56
25G	0.29	0.51
26G	0.25	0.46
27G	0.20	0.41

Table S4: Cut-off diameter of the Andersen Cascade Impactor at flow rate 28.3 L/min.

Stages	Cut-off diameter
0	9.0
1	5.8
2	4.7
3	3.3
4	2.1
5	1.1
6	0.7
7	0.4
8	0.0

Table S5: Infusion rate of pulmonary drug delivery devices

Device	Study on	Infusion rate	Reference
Vibrating mesh nebulizer	Veletri (epoprostenol)	8.4 – 19.6 (mL/h)	[7]
Vibrating mesh nebulizer	Sodium chloride, albuterol, epoprostenol	12 (mL/h)	[8]
Jet nebulizer	Prostacyclin (PGI$_2$)	8 (mL/h)	[9]
Jet nebulizer	^{99m}Tc-saline	1.5 – 12 (mL/h)	[10]
Jet nebulizer	Normal saline	Low: 15 – 16.6 (mL/h) High: 37.7 – 46 (mL/h)	[11]
Vibrating mesh nebulizer	Albuterol powder	4-20 (mL/h)	[12]
Jet nebulizers	Abuterol and Saline	7.5 – 25 (mL/h)	[13]
Vibrating mesh nebulizer	Radiolabeled saline	1.5 – 12 (mL/h)	[14]
Jet nebulizer and vibrating nebulizer	Radiolabeled saline	5-10 (mL/h)	[15]
Bipoler atomisation	PVDF polymer	1 – 10 (mL/h)	This study

Table S6: Release kinetics of PVDF 3% - CUR 1.5% and PVDF 3% - CUR 3% applied on common mathematic models.

Fitting models	PVDF@CUR1.5 (pH 7.4)		PVDF@CUR3 (pH 7.4)	
	Regression equations	R^2	Regression equations	R^2
Zero-order	$Q = 0.0071\ t + 0.3593$	0.7068	$Q = 0.0087\ t + 0.4053$	0.7237
First-order	$\log Q = 0.0065\ t - 0.4706$	0.5345	$\log Q = 0.0068\ t - 0.4147$	0.5865
Higuchi	$Q = 7.4965\ t^{1/2} + 21.7696$	0.8842	$Q = 9.2066\ t^{1/2} + 23.1778$	0.9020
Hixon–Crowell	$Q^{1/3} = -0.0191\ t + 4.0016$	0.8102	$Q^{1/3} = -0.0291\ t + 3.9171$	0.8569
Korsmeyer–Peppas	$\log Q = 0.4463\ \log t - 0.7095$	0.9705	$\log Q = 0.4003\ \log t - 0.6333$	0.9881

Table S7: Performance evaluation (Mass mean aerodynamic diameter - MMAD, geometric standard deviation - GSD, fine particle fraction - FPF) of the bipolar atomization and other devices with Andersen Cascade Impactor test.

Device	Deposition in ACI (%)	MMAD (µm)	GSD	FPF (%)	References
Bipolar atomization	80.8	2.18 ± 0.17	2.66 ± 0.24	72.98 ± 0.83	This work
MDI (0.16 mm actuator)	70.2	1.2	n/a	75.1	[16]
MDI (0.28 actuator)	33.3	1.3	n/a	34.0	[16]
MDI (Albuterol Sulfate)	74	2.4	1.8	67	[17]
MDI (Ipratropium Bromide)	72	3	1.6	64	[17]
MDI	50.5	n/a	n/a	42.3	[18]
Jet nebulizer (NaF aerosol)	10	2.6	n/a	n/a	[19]
Jet nebulizer (Terbutaline)	2.3	2.1	n/a	n/a	[19]
Vibrating mesh nebulizer	3.9	3.3	n/a	n/a	[19]
PMDI	0.6	3.1	n/a	n/a	[19]
DPI	1.5	3.2	n/a	n/a	[19]
Mesh nebulizer (Normal saline)	n/a	5.54	1.89	42.85	[20]
Mesh nebulizer (Normal saline)	n/a	4.78	1.97	51.4	[20]
Air-jet nebulizer (Normal saline)	n/a	5.72	1.8	36.07	[20]
Ultrasonic nebulizer (Normal saline)	n/a	4.63	1.77	56.66	[20]
Jet nebulizer	3 – 6	0.87	1.62	n/a	[21]
Air-Jet Nebulizer	n/a	2.53	2.76	n/a	[22]

References

[1] J. Melcher, G. Taylor, Electrohydrodynamics: a review of the role of interfacial shear stresses, Annual review of fluid mechanics 1(1) (1969) 111-146, https://doi.org/10.1146/annurev.fl.01.010169.000551.

[2] J.U. Brackbill, D.B. Kothe, C. Zemach, A continuum method for modeling surface tension, J. Comput. Phys. 100(2) (1992) 335-354, https://doi.org/10.1016/0021-9991(92)90240-Y.

[3] C.W. Hirt, B.D. Nichols, Volume of fluid (VOF) method for the dynamics of free boundaries, J. Comput. Phys. 39(1) (1981) 201-225, https://doi.org/10.1016/0021-9991(81)90145-5.

[4] H. Huh, R.E. Wirz, Simulation of electrospray emission processes for low to moderate conductivity liquids, Physics of Fluids 34(11) (2022), https://doi.org/10.1063/5.0120737.

[5] G. Tomar, D. Gerlach, G. Biswas, N. Alleborn, A. Sharma, F. Durst, S.W.J. Welch, A. Delgado, Two-phase electrohydrodynamic simulations using a volume-of-fluid approach, J. Comput. Phys. 227(2) (2007) 1267-1285, https://doi.org/10.1016/j.jcp.2007.09.003.

[6] J.R. Melcher, Continuum electromechanics / James R. Melcher, MIT Press, Cambridge, Mass, 1981.

[7] A.C. Anderson, M.N. Dubosky, K.A. Fiorino, V. Quintana, C.A. Kaplan, D.L. Vines, The effect of nebulizer position on aerosolized epoprostenol delivery in an adult lung model, Respiratory Care 62(11) (2017) 1387-1395.

[8] K. McDermott, J.G. Oakley, Droplet size and distribution of nebulized 3% sodium chloride, albuterol, and epoprostenol by phase Doppler particle analyzer, Current Therapeutic Research 94 (2021) 100623, https://doi.org/10.1016/j.curtheres.2021.100623.

[9] M.S. Siobal, R.H. Kallet, J.-F. Pittet, E.L. Warnecke, R.W. Kraemer, R.V. Venkayya, J.F. Tang, Description and evaluation of a delivery system for aerosolized prostacyclin, Respiratory Care 48(8) (2003) 742-753.

[10] M. McPeck, G.C. Smaldone, Continuous infusion aerosol delivery of prostacyclins during mechanical ventilation: challenges, limitations, and recent advances, Expert Opinion on Drug Delivery 19(5) (2022) 465-474, https://doi.org/10.1080/17425247.2022.2061460.

[11] C. Reisner, J. Lee, A. Kotch, G. Dworkin, Comparison of volume output from two different continuous nebulizer systems, Annals of Allergy, Asthma & Immunology 76(2) (1996) 209-213, https://doi.org/10.1016/S1081-1206(10)63424-2.

[12] J. Li, W. Wei, J.B. Fink, In vitro comparison of unit dose vs infusion pump administration of albuterol via high-flow nasal cannula in toddlers, Pediatric Pulmonology 55(2) (2020) 322-329, https://doi.org/10.1002/ppul.24589.

[13] G.B. Moody, A. Ari, Quantifying continuous nebulization via high flow nasal cannula and large volume nebulizer in a pediatric model, Pediatric Pulmonology 55(10) (2020) 2596-2602, https://doi.org/10.1002/ppul.24967.

[14] M. McPeck, S. Ashraf, A.D. Cuccia, G.C. Smaldone, Factors determining continuous infusion aerosol delivery during mechanical ventilation, Respiratory Care 66(4) (2021) 573-581, https://doi.org/10.4187/respcare.07715.

[15] J.A. Lee, M. McPeck, A.D. Cuccia, G.C. Smaldone, Real-time analysis of dry-side nebulization with heated wire humidification during mechanical ventilation, Respiratory Care 67(8) (2022) 914-928, https://doi.org/10.4187/respcare.09459.

[16] S. Hou, R.N. Anderson, K. Kriesel, A. Bodria, D. Copelli, Comparison of Andersen and next generation impactors on aerodynamic sizing of a solution metered dose inhaler (MDI) tested with different orifice diameter actuators, Respir Drug Deliv Eur Proc (2007) 217-220.

[17] C. Guo, S.R. Gillespie, J. Kauffman, W.H. Doub, Comparison of delivery characteristics from a combination metered-dose inhaler using the Andersen cascade impactor and the next generation pharmaceutical impactor, Journal of pharmaceutical sciences 97(8) (2008) 3321-3334, https://doi.org/10.1002/jps.21203.

[18] J. Mitchell, M. Nagel, V. Avvakoumova, H. MacKay, R. Ali, The abbreviated impactor measurement (AIM) concept: part 1—influence of particle bounce and re-entrainment—evaluation with a "dry" pressurized metered dose inhaler (pMDI)-based formulation, Aaps Pharmscitech 10 (2009) 243-251, https://doi.org/10.1208/s12249-009-9202-9.

[19] C. Majoral, A.L. Coates, A. Le Pape, L. Vecellio, Humidified and heated cascade impactor for aerosol sizing, Frontiers in Bioengineering and Biotechnology 8 (2020) 589782, https://doi.org/10.3389/fbioe.2020.589782.

[20] O. Mišík, J. Kejíková, O.e. Cejpek, M. Malý, A. Jugl, M. Bělka, F. Mravec, F. Lizal, Nebulization and in vitro upper airway deposition of liposomal carrier systems, Molecular Pharmaceutics 21(4) (2024) 1848-1860, https://doi.org/10.1021/acs.molpharmaceut.3c01146.

[21] K.P. Fennelly, M.D. Tribby, C.-Y. Wu, G.L. Heil, L.J. Radonovich, J.C. Loeb, J.A. Lednicky, Collection and measurement of aerosols of viable influenza virus in liquid media in an Andersen cascade impactor, Virus Adaptation and Treatment (2014) 1-9, https://doi.org/10.2147/VAAT.S74789.

[22] O. Misik, A. Peštálová, M. Belka, F. Lízal, Nebulizer particle size distribution measured by various methods, EPJ Web of Conferences, EDP Sciences, 2022, p. 01023, https://doi.org/10.1051/epjconf/202226401023.